ABSTRACT

PRACTICAL VORTEX BEAM GENERATION

by
Nedime Pelin Mohamed Hassan Salem

Vector vortex beams are monochromatic electromagnetic wave fields carrying spin angular momentum (SAM) and orbital angular momentum (OAM). Spin angular momentum is associated with the polarization of the field, whereas OAM yields an azimuthal field dependence of the form $\exp(jq\phi)$, where ϕ is the azimuthal angle, and q is an integer designating the helicity order, which is also known as the topological charge of the vortex beam. Vortex beams owe their names to the characteristic on-axis phase singularity and amplitude null.

In this study, a new method to generate vector vortex beams in the microwave regime is devised based on waveguide modes, where the vortex beam is set to be the aperture field at the open-end of a metallic circular waveguide section. This method takes inspiration from previous work on zero-order Bessel beam generation in the microwave regime. In this design, the launched vortex beam is a transverse electric (TE) electromagnetic field with a truncated Bessel profile. The aperture field is formed by the propagating field of the TE_{q1} mode of the waveguide. Excitation is provided by means of a single circular loop antenna inserted coaxially inside the waveguide section. The waveguide housing of the large loop antenna is shown to be advantageous in terms of impedance matching, where the input impedance is shown to depend on the antenna location inside the waveguide. A phenomenological simplified analytical expression of

the input impedance is derived based on transmission-line theory and verified using multi-level fast multipole method (MLFMM) full-wave simulation. In the far-field region, vortex beams have conical radiation pattern, and by adding an angled flange to the waveguide, the radiation cone angle can be altered. In particular, the effect of the flange angle on the direction of the maximum radiation is studied to provide valuable insight into using the launcher in practical communication links. Furthermore, a parametric sensitivity analysis is performed to model the effect of small perturbations in antenna position and tilt on the performance of the launcher.

This research aims to provide a practically feasible method for vortex beam generation in the microwave regime; however, due to practical limitations, the results of this research are not yet compared to experimental data, but are numerically verified using full-wave simulations.

PRACTICAL VORTEX BEAM GENERATION

by
Nedime Pelin Mohamed Hassan Salem

A Dissertation
Submitted to the Faculty of
New Jersey Institute of Technology
in Partial Fulfillment of the Requirements for the Degree of
Doctor of Philosophy in Electrical Engineering

Helen and John C. Hartmann Department of
Electrical and Computer Engineering

August 2018

.

APPROVAL PAGE

PRACTICAL VORTEX BEAM GENERATION

Nedime Pelin Mohamed Hassan Salem

Dr. Edip Niver, Dissertation Advisor Date
Professor of Electrical and Computer Engineering, NJIT

Dr. Peter Petropoulos, Committee Member Date
Associate Professor of Mathematical Sciences, NJIT

Dr. Ali Akansu, Committee Member Date
Professor of Electrical and Computer Engineering, NJIT

Dr. Gerald Whitman, Committee Member Date
Professor of Electrical and Computer Engineering, NJIT

Dr. Ali Abdi, Committee Member Date
Professor of Electrical and Computer Engineering, NJIT

BIOGRAPHICAL SKETCH

Author: Nedime Pelin Mohamed Hassan Salem

Degree: Doctor of Philosophy

Date: August 2018

Undergraduate and Graduate Education:

- Doctor of Philosophy in Electrical Engineering,
  New Jersey Institute of Technology, Newark, NJ, 2018

- Master of Science in Electrical Engineering,
  New Jersey Institute of Technology, Newark, NJ, 2009

- Bachelor of Science in Electrical and Electronics Engineering,
  Blacksea Technical University, Trabzon, Turkey, 2005

Major: Electrical Engineering

Publications:

N. Pelin M. H. Salem, Edip Niver, and Mohamed A. Salem, "*Impedance Matching of a Large Loop Antenna Inside a Circular Waveguide*," Proceedings of the 2018 IEEE International Symposium on Antennas and Propagation & USNC/URSI National Radio Science Meeting, Boston, MA, pp. TBD, July 2018.

N. Pelin M. H. Salem, Edip Niver, and Mohamed A. Salem, "*Flange Angle Design for Waveguide-Based Orbital Angular Momentum Multiplexing Communication Systems*," Proceedings of the 2018 Asia-Pacific Microwave Conference, Kyoto, Japan, pp. TBD, November 2018.

N. Pelin M. H. Salem, Edip Niver, and Mohamed A. Salem, "*Sensitivity Analysis of Input Impedance of a Large Loop Antenna in a Waveguide to Tilt Angle*," Proceedings of the 2018 Asia-Pacific Microwave Conference, Kyoto, Japan, pp. TBD, November 2018.

N. Pelin M. H. Salem, Edip Niver, and Mohamed A. Salem, "*Microwave Vortex Beam Launcher Design*," IET Journal on Microwaves, Antennas & Propagation, pp. TBD (ACCEPTED).

To my daughter, Lal and my husband, Mohamed,
who constantly inspire me to be a better version of myself

ACKNOWLEDGMENT

I would like to express my deepest appreciation to Dr. Edip Niver, who not only served as my research supervisor, providing valuable insight and intuition, but also giving me constant support and encouragement. Special thanks are given to Dr. Peter Petropoulos, Dr. Ali Akansu, Dr. Gerald Whitman, and Dr. Ali Abdi for actively participating in my committee.

I would like to express my deep gratitude to my husband, Dr. Mohamed Salem for providing valuable feedback, insight, and intuition, and also constantly giving me support, encouragement, and reassurance. I wish to thank Oksana Manzhura for her assistance and friendship during the course of my study. Finally, I would like to express my deepest gratitude to my daughter, Lal Salem and all my family members for their love and support.

TABLE OF CONTENTS

TABLE OF CONTENTS
(Continued)

LIST OF TABLES

Table **Page**

LIST OF FIGURES

LIST OF FIGURES
(Continued)

LIST OF FIGURES
(Continued)

Figure **Page**

LIST OF SYMBOLS

ν	Mode index
q	Topological charge
c	Speed of light ($\sim 3\times10^{8}$ m/s)
ε_0	Free-space permittivity ($\sim 8.85\times10^{-12}$ F/m)
μ_0	Free-space permeability ($4\pi\times10^{-7}$ H/m)
$\hbar$	Planck's constant ($\sim 6.63\times10^{-34}$ m^2kg/s)
∂	Partial differential
∇	Nabla (or del)
∇^2	Laplacian
λ	Wavelength
k	Wavenumber
χ	Transverse wavenumber
β	Longitudinal wavenumber
γ	Propagation constant

CHAPTER 1

INTRODUCTION

1.1 Objective

The objective of this dissertation is to present a novel launching structure for vortex beam generation in the microwave regime. The practical aspects relevant to realizing the structure, including antenna impedance matching, effect of the geometry on radiation pattern, and performance sensitivity to perturbations in certain design parameters are studied.

First, the structure of the launcher is proposed as a combination of a coaxially-fed large loop antenna coaxially placed inside a metallic circular waveguide section. Next, modal analysis is performed using the relationship between the waveguide modes and the known antenna current to determine the corresponding amplitudes for the excited transverse electric (TE) and transverse magnetic (TM) modes. Upon establishing the relationship between the antenna current and the amplitudes of the excited modes, the antenna current is set such that the excited modes form a vortex beam when launched into free-space.

The study provides a flexible and systematic method to design a vortex beam launcher that is also feasible for commercial and industrial implementation. To this end, the study provides a comprehensive, accurate and simplified approach to optimize the performance of the launcher. Additionally, parametric sensitivity analysis is performed to determine how perturbations to the launcher geometry,

which may occur due to manufacturing tolerances, affect the quality of the generated vortex beam.

1.2 Vortex Beams and OAM

All propagating electromagnetic waves carry energy, which is related to how the electromagnetic field varies in time and space. Electromagnetic waves also carry momentum, which has two components. One component, the linear momentum, is related to the translational dynamics of the wave, that is, its wave-vector. The other momentum component is the angular momentum, which is further divided into two parts: (i) spin angular momentum (SAM), which determines the polarization of the electromagnetic field, and (ii) orbital angular momentum (OAM), which determines the phase helicity or the vorticity of the wave. Similar to energy and linear momentum, the total angular momentum of the electromagnetic wave is conserved. This suggests that SAM may be converted into OAM, and vice versa.

The general expression of a vortex beam, which is a wave carrying OAM, in the cylindrical coordinate system (ρ, ϕ, z) may be expressed as

$$E_v(\rho, \phi, z, t) = U(\rho; q, \beta, \omega) e^{jq\phi} e^{-j\beta z} e^{j\omega t}, \tag{1.1}$$

where β is the longitudinal wavenumber and ω is the angular frequency. The term $e^{-j\beta z} e^{j\omega t}$ implies a monochromatic wave propagating in the $+z-$direction. The function $U(\rho; q, \beta, \omega)$ defines the radial profile of the wave. If the profile is localized in space, that is, most of the amplitude is concentrated in a well-defined region, then such wave is called a “beam”. The remaining term defines the azimuthal (or angular)

dependence, where q is an integer, called the topological charge, and determines the OAM-state of the beam.

For OAM-state 0, the wave has no vorticity and its phase progresses as disconnected planes. This can be observed in plane-waves for example or in conventional Gaussian beams. A beam that carries OAM has a phase that progress like a helix or a spiral staircase. The sign of the topological charge determines the sense of rotation of this spiral relative to the direction of propagation. A positive sign corresponds to a left-handed spiral whereas a negative sign corresponds to a right-handed spiral. The magnitude of q determines the number of "turns" per longitudinal wavelength. For example, for $q = 4$, the phase spirals four times over a distance of λ along the z-axis. The phase is not defined at $\rho = 0$. This discontinuity in the phase results in a characteristic null in the amplitude at the center of all vortex beams. Figure 1.1 illustrates the magnitude and phase of beams carrying different topological charges. The left column depicts three-dimensional (3D) plots of the phase-front for different topological charges, while the center and right columns respectively show two-dimensional (2D) plots of the corresponding phase and magnitude in a plane transverse to the direction of propagation. The helical phase structure and its handedness is clearly illustrated in the 3D phase plots, whereas the characteristic phase discontinuity and amplitude null at the center are visualized in the 2D plots.

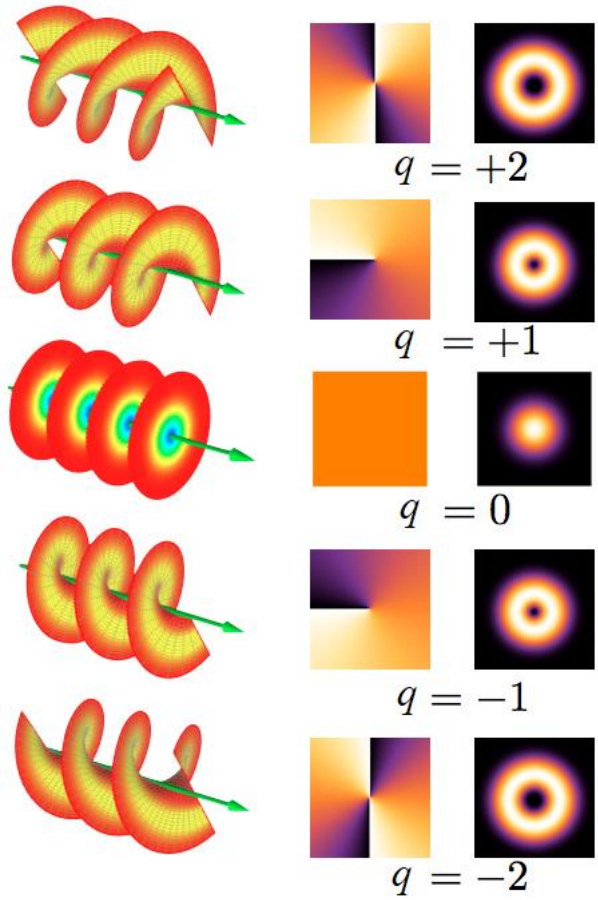

Figure 1.1 Illustration of propagating beams with the topological charges $q = 0, \pm 1, \pm 2$. The 3D plots illustrate the helical structure and the handedness of the phase fronts for beams propagating in the direction of the green arrow, while the 2D plots depict the phase and magnitude in a plane transverse to the direction of propagation.

Source: Wikimedia Commons, accessed July 24, 2018.

1.3 OAM Applications

The early work of Poynting [1] illustrated that angular momentum, which is the spin of individual photons, can be attributed to a circularly polarized light beam. Later in 1932, it was found that in higher-order atomic transitions, photons carry angular momentum exceeding that prescribed for polarization [2]. This additional angular momentum is called "orbital angular momentum" (OAM). In 1992, Allen *et al.*

established that photons carrying OAM form light beams with helical phase fronts [3].

The importance of Allen's work was establishing a link between beams with helical phase-fronts and OAM for the first time. However, this was not the first instance beams with helical phase-fronts were produced or studied in the literature. Such beams were known as "optical vortices" [4] and various approaches for producing them were already known.

One of the very first published methods to produce OAM is by using cylindrical lenses to transform higher-order Hermite-Gaussian modes emitted by a typical laser into Laugerre-Gaussian modes with helical phase-fronts [5]. Another commonly used early method to generate OAM is allowing a conventional laser beam to pass through a spiral phase plate, which is a dielectric plate with a thickness that increases with azimuthal angle and thus introduces helicity to the phase-front of the laser beam [6]. Employing a pitchfork hologram to generate OAM is another innovative method developed by Soskin *et al.* in 1990. The technique involves a diffraction grating containing a q-pronged fork dislocation in the ruled lines to add OAM with order q to the incident beam [7]. It is worth noting that using this technique results in splitting of the incident beam into two diffracted beams carrying OAM with opposite signs.

Diffractive optical elements can only work for a single frequency that is defined by design and they are not useful if a broadband beam is desired. Custom optical elements can use Fresnel reflections to introduce a localized phase shift, hence enabling the generation of wide-band vortex beams [8].

As it can be seen from these examples, most of the generation methods made use of optical elements to convert laser beams into vortex beams. These methods are now easily implemented using computer controlled spatial light modulators (SLM) as reconfigurable optical elements [9]. Spatial light modulators are increasingly replacing previously used diffractive optical elements. The most common SLM material used for OAM applications is a liquid crystal thin film whose refractive index can be locally switched by applying an electric field. The films are then laid over computer-controlled pixelated electronic arrays to generate local phase variations [10].

It is also shown that the generation of vortex beams on chip is possible by the development of chip-scale sources relying on the vertical emission from ring waveguides with small slots on them as scattering centers [11].

Since their inception, vortex beams found plenty of applications in optical manipulation. In 1995, Rubinsztein-Dunlop *et al.* proposed to add OAM to optical tweezers, which are single highly-focused laser beams capable of trapping a microscopic particle in a specific location in space. Rubinsztein-Dunlop *et al.* used a diffractive optical element to produce a third-order OAM-carrying beam and coupled this beam into an optical tweezer to trap an absorbing particle. The linear momentum of the light beam pushed the absorbing particle to a cover slip and the angular momentum of the beam set the particle spinning around its own axis. This work is the first introduction of an OAM transfer from light to a microscopic object [12]. In 2002, Grier *et al.* introduced a “holographic optical tweezer” by using a programmable SLM to switch between different beam types and steer multiple beams

independently of each other [13]. This work started a new era of using structured beams within optical tweezers and using SLMs more frequently for beam-shaping purposes [14, 15].

Although OAM-carrying waves were originally used in optical fields, yet generally speaking, phase singularities occur when three or more plane-waves interfere [16]. Such property extends the domain of applicability of OAM-carrying waves to electromagnetic and acoustic fields, too. Moreover, helical phase-fronts were also demonstrated in OAM-carrying electron beams [17 - 19].

The angular Doppler shift phenomenon is observed in OAM-carrying waves. In conventional (linear) Doppler shift, reflection from a linearly moving object induces frequency shift proportional in magnitude to the velocity, while the direction of motion affects the sign of the shift. In angular Doppler shift, reflection of OAM-carrying waves from a rotating object induces frequency shift proportional in magnitude to the rotational velocity, while the direction of rotation and the handedness of the OAM-state determine the sign of the shift. The angular Doppler shift can thus be used to measure the rotational velocity of small particles through the detection of frequency-shifted components of circularly polarized light scattered from such particles, the sign of the shift indicating the sense of the particle rotation [20].

Orbital angular momentum is widely researched in the field of quantum mechanics. Zeilinger *et al.* performed the first single-photon based OAM experiment examining quantum entanglement of two photons both carrying OAM [21]. In 2002, the same research team demonstrated a method to detect OAM modes using

superposition of Laugerre-Gaussian modes, which is significant for quantum cryptography applications with higher alphabets that could enable increased data rates [22].

Orbital angular momentum has also found applications in astronomy. In 2008, Swartzlander *et al.* demonstrated the application of OAM in a coronagraph to enhance observation of individual stellar objects by filtering out the interference from neighboring bright stellar objects that are placed in the dark null of a formed vortex beam [23].

Orbital angular momentum is widely explored is the field of imaging. In 2005, Furhapter *et al.* employed OAM-carrying beams in spiral interferometry and successfully introduced depth perception into 2D molecular imaging which greatly reduced the time and efforts spent on imaging [24]. More sophisticated OAM based filters can give accurate information on depth [25] and even introduce the ability to fully reconstruct the 3D images from a single scan of the sample [26].

By far, the most active research field with most controversy for OAM use is wireless communications. In 2012, Tamburini *et al.* published the results of their Venice experiment, the first long distance OAM multiplexing scheme over a radio communication link with a length of 442 m (3536λ) [27]. Shortly thereafter, Tamagnone *et al*. raised concerns claiming that the experiment did not demonstrate new results and what was demonstrated is a subset of conventional Multiple Input Multiple Output (MIMO) spatial diversity technique. They further claimed that OAM multiplexing cannot work over long distances since it is a near-field phenomenon [28]. Tamburini *et al.* responded [29] by clarifying that the physical concepts behind

MIMO and OAM are very different (as discussed in section 1.3). Spatial diversity, the principle enabling MIMO, is related to the linear momentum of the electromagnetic field, whereas OAM multiplexing is enabled by utilizing the angular momentum of the field. Moreover, Tamburini *et al.* showed that the operation range is equivalent to MIMO and OAM states can be recovered in the far-field.

After Tamburini *et al.*'s demonstration, many research groups published additional work and demonstrations using OAM modes in wireless communications. In 2014, Yan *et al.* published their work on a 32-Gbps mm-wave link over 2.5 m with high spectral efficiency using four independent channels [30]. The channels are formed by multiplexing two OAM-states with polarization diversity. They successfully demonstrated that the multiplexed beams require only a single aperture for the transmitter and similarly a single aperture for the receiver (although with certain minimum aperture sizes). Moreover, OAM-state orthogonality is used to achieve efficient demultiplexing without additional digital signal post-processing to cancel channel interference. In 2015, Hui *et al.*, experimentally demonstrated a dual OAM-state antenna using a 60 GHz wireless communication link with two separate OAM channels and transmitted high-definition video signals over a distance of 1.4 m [31].

Although the research community is strongly polarized about OAM multiplexing in free-space, there is almost a consensus on the usefulness of OAM multiplexing in guided systems. In 2015, Li *et al.* experimentally evaluated the performance of analog signal transmission in an OAM multiplexing system through fiber [32]. They concluded that the established 8-OAM multiplexing system shows

low inter-mode crosstalk, which benefits high-quality analog performance. In 2018, Zhu *et al*. reported on their design and fabrication of a graded-index ring-core fiber and experimental demonstration of 8.4 Tbit/s data transmission in an 18 km OAM fiber with low crosstalk [33].

Orbital angular momentum multiplexing, which introduces an additional multiplexing degree of freedom along with time, space, frequency, and code, may thus be employed separately or in conjunction with any of the other multiplexing techniques to further increase communication data capacity. Several technical challenges still need to be addressed before OAM multiplexing can become an industrial communication standard [34, 35], which further emphasizes the importance of investigating practical vortex beam generation and detection methods.

1.4 Previous Work

In this section, the main concepts employed to generate vortex beams and their recent implementations are reviewed.

One of the commonly used devices to generate vortex beams, especially in the optical regime is the spiral phase plate (SPP). An SPP is a transparent dielectric plate with non-uniform thickness. An input wave slows down in optically dense media, taking more time to cover a given distance inside the media than outside in air. The thickness profile of the SPP itself is helical. A light beam passing through the SPP acquires local phase shift that depends on the angle, which introduces vorticity in its phase-front [36]. Figure 1.2 illustrates the concept of vortex beam generation using an SPP. A beam with a planar phase-front impinges on the SPP and

emerges as a helical beam. The impinging beam acquires local phase proportional to the local thickness of the plate. Note that the maximum thickness difference of the SPP, d, determines the additional OAM added to the impinging beam as $|q| = n_{\mathrm{SPP}} d/\lambda$, where n_{SPP} is the refractive index of the SPP.

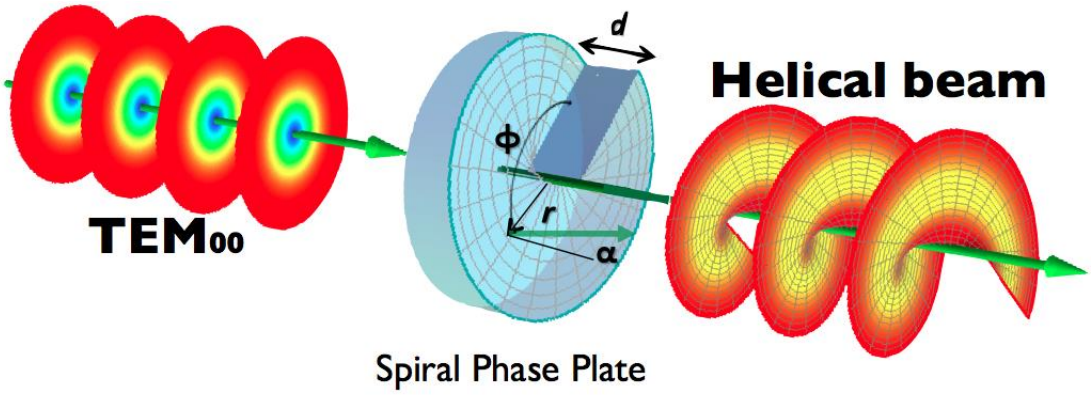

Figure 1.2 Illustration of vortex beam generation concept using a spiral phase plate. The impinging beam is a transverse electromagnetic beam, TEM_{00}, and carries no OAM. The beam acquires local phase proportional to the local thickness of the SPP and emerges as a helical beam.

Source: Wikimedia Commons, accessed July 24, 2018.

Another commonly used method is employing computer generated pitch-fork holograms (PFH). A wave passing through a PFH splits into two OAM-carrying waves [37]. In most common configurations, the incident wave carries no OAM, while the emerging waves carry OAM with equal in magnitude and opposite in sign topological charges. Figure 1.3 illustrates the concept of vortex beam generation using PFH. A planar beam impinges on the PFH and is split into two beams carrying OAM. The emerging beams are in OAM states with opposite signs. The OAM order itself is the result of the specific hologram design. Note that due to the conservation

of the total OAM, the OAM of both emerging beams is equal to that of the impinging beam.

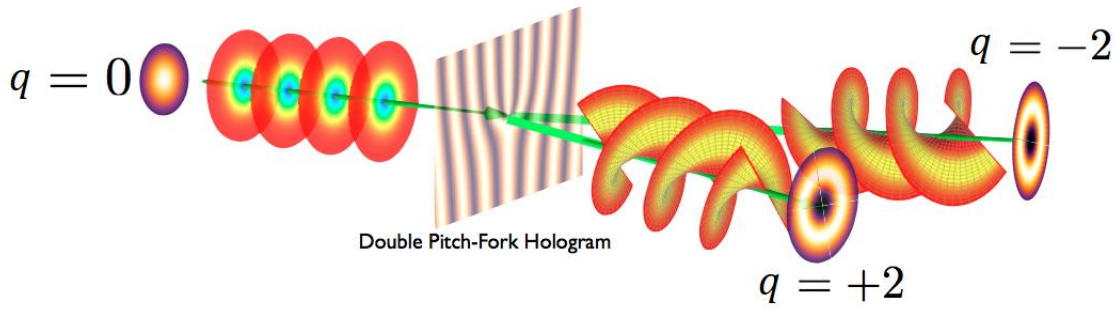

Figure 1.3 Illustration of vortex beam generation concept using pitch-fork hologram. The impinging beam carries no OAM and is split into two helical beams carrying OAM of order 2 and opposite signs. The sum of OAM of the emerging beams is equal to that of the impinging beam due to OAM conservation.

Source: Wikimedia Commons, accessed July 24, 2018.

Another common method employs Q-plates. A Q-plate is a bi-refringent dielectric plate with a locally varying refractive index profile. For instance, a right-handed circularly polarized wave passing through a Q-plate may be transformed into a left-handed circularly polarized wave and acquires a topological charge and, consequently, a helical phase. Q-plates demonstrate that SAM and OAM can be converted from one form into the other [38]. Figure 1.4 illustrates the concept of vortex beam generation using Q-plates. An impinging circularly polarized beam changes its polarization handedness and acquires OAM.

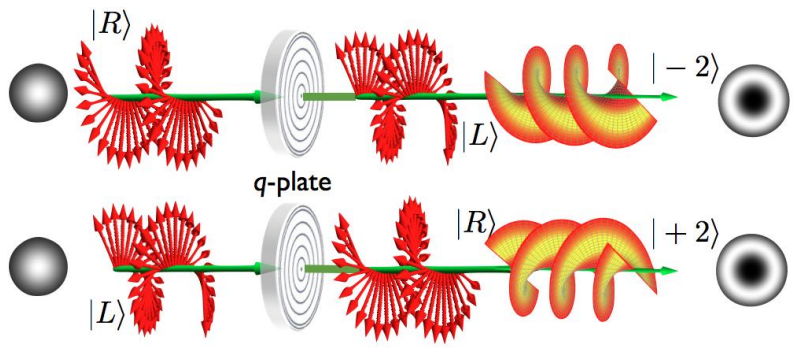

Figure 1.4 Illustration of vortex beam generation concept using a Q-plate. An impinging circularly polarized beam changes its polarization handedness and acquires OAM. Note that the red arrows represent field orientation, while the helical planes represent phase fronts. The beam magnitude in a plane transverse to the direction of propagation is depicted in black and white on the left for impinging beams, and on the right for emerging beams.

Source: Wikimedia Commons, accessed July 24, 2018.

In addition to the aforementioned generation techniques in the optical regime, some vortex beam generation techniques are recently reported in the radio frequency and millimeter-wave regime. In 2013, Deng *et al.* implemented a circular Vivaldi antenna array of eight elements to generate vortex beams at 6 GHz with topological charges $\pm1, \pm2, \pm3, \pm4$, by feeding the antennas with equal amplitudes and successive phase shifts [39]. The idea is sound, however, what is generated and reported in this publication are not proper OAM modes. The vorticity is demonstrated in the field amplitude, not in the phase. The characteristic amplitude null at the center of the beam is also missing.

In 2016, Byun et al. implemented a cassegrain reflector antenna to generate three OAM modes simultaneously as a part of an OAM multiplexing system [40]. The operation frequency of the system is 18 GHz with varying link distances up to 2.5 m. The implemented structure is quite complex and the purity of the generated OAM

modes is low because the phase is sampled only in four points (four sectors). This system resembles a very crude SPP.

In 2017, Kou *et al.* implemented a system employing metasurfaces to generate a vortex beam with topological charge 2 at 10 GHz [41]. The metasurface is composed of elements that change the phase of the incident wave locally, so the metasurface practically behaves as a flat SPP.

1.5 Organization

The organization of this dissertation is as follows: Chapter 2 gives a detailed introduction to electromagnetic vortex beams and the theoretical framework of this dissertation. Chapter 3 provides details on the novel launcher design and its theory of operation. Chapter 4 investigates the practical aspects of the design, including optimal impedance matching design, effect of adding an angled flange on the launcher radiation pattern, and a parametric sensitivity analysis on the effect of geometrical perturbations on the launcher performance. Chapter 5 draws conclusions of this study, lists the limitations of performed analyses, and suggests potential future work.

CHAPTER 2

ELECTROMAGNETIC VORTEX BEAMS

2.1 Introduction

In this chapter, the structure and physical properties of the vortex beams are studied. Vector vortex beams are monochromatic electromagnetic fields carrying spin angular momentum and orbital angular momentum. Spin angular momentum is associated with the polarization of the field, whereas OAM yields an azimuthal field dependence of the form $\exp(\pm jq\phi)$, where ϕ is the azimuthal angle and q is an integer designating the topological charge of the vortex beam [3,50]. Vortex beams owe their names to the characteristic on-axis phase singularity and amplitude null [42]. There are different types of vortex beams, however in this chapter, and in this work in general, the Bessel type, which emerge as the fundamental solution of the wave equation in cylindrical coordinates with no azimuthal symmetry, is studied. The dynamics of such beams are discussed after deriving their form (in terms of momentum and energy). And lastly, the other types of vortex beams used in various theoretical and experimental investigations are briefly introduced.

2.2 Structure of Vortex Beams

In this section, the fundamental physics of vortex beams are explored in terms of their spectral structure. First the spectral structure of Bessel beams are explored, then the general expression of Bessel vortex beams are studied. Bessel beams belong to a class of waves called propagation-invariant beams. Such beams exhibit four essential

physical characteristics: (i) being monochromatic waves, (ii) propagating along a well-defined axis, (iii) propagating without distortion in their transverse profile and with harmonic phase variation along their propagation axis, and (iv) their energy concentrated in a localized region in the transverse plane, namely having a beam 'spot'. Specifically, scalar Bessel beams are eigensolutions of the source-free scalar wave equation in the circular cylindrical coordinate system.

The source-free wave equation in free-space is

$$\left[\nabla^2 - \frac{\partial^2}{c^2 \partial t^2}\right]\Psi(\mathbf{r},t) = 0, \tag{2.1}$$

where ∇^2 is the Laplacian, Ψ is the wave function, $\mathbf{r}$ is the position vector, and c is the speed of light in free-space. To find the eigensolutions to Equation (2.1), which are of interest, the method of separation of variables is used. Let $\Psi(\mathbf{r},t) = R(\mathbf{r})T(t)$, where $R(\mathbf{r})$ is space-dependent term and $T(t)$ is the time-dependent term. Since monochromatic waves are the sole interest, time-dependent term is fixed as $T(t) = \exp(j\omega t)$, where ω is the angular frequency of the beam. Substituting $\Psi(\mathbf{r},t) = R(\mathbf{r})\exp(j\omega t)$ into Equation (2.1) yields the homogeneous Helmholtz equation

$$\left[\nabla^2 + k^2\right]R(\mathbf{r}) = 0, \tag{2.2}$$

where $k = \omega / c$ is the wave-number. Equation (2.2) is not written in any specific coordinate system, however the Bessel eigensolutions in the circular cylindrical coordinate system are sought [43].

The Laplacian in Equation (2.2) is separated in a transverse term and a longitudinal term as $\nabla^2 = \nabla_\perp^2 + \partial_z^2$. Accordingly, the space-dependent function can be also separated in transverse and longitudinal terms as $R(\mathbf{r}) = R_\perp(\boldsymbol{\rho})Z(z)$, where $\boldsymbol{\rho}$ is the transverse position vector and $Z(z)$ is the longitudinal space-dependent term, which is chosen as the propagation axis. Similar to the time-dependent term, the longitudinal term is fixed to $Z(z) = \exp(-j\beta z)$, where β is the longitudinal component of the wave-vector. Substituting back into Equation (2.2) yields

$$\left[\nabla_\perp^2 + \chi^2\right] R_\perp(\boldsymbol{\rho}) = 0, \tag{2.3}$$

with $\chi^2 = k^2 - \beta^2$, the transverse component of the wave-vector. The transverse Laplacian operating on $R_\perp(\boldsymbol{\rho})$ in the circular cylindrical coordinate system results in

$$\nabla_\perp^2 R_\perp(\rho,\phi) = \frac{\partial}{\rho\partial\rho}\left[\rho\frac{\partial R_\perp(\rho,\phi)}{\partial\rho}\right] + \frac{\partial^2 R_\perp(\rho,\phi)}{\rho^2\partial\phi^2}. \tag{2.4}$$

Further using separation of variables, the transverse term is expressed as $R_\perp(\rho,\phi) = U(\rho)\Phi(\phi)$, where $U(\rho)$ is the radial dependency term and $\Phi(\phi)$ is the azimuthal (angular) dependency term, respectively. Rewriting Equation (2.3) using this new expression yields

$$U''(\rho)\Phi(\phi) + \frac{1}{\rho}U'(\rho)\Phi(\phi) + \frac{1}{\rho^2}U(\rho)\Phi''(\phi) + \chi^2 U(\rho)\Phi(\phi) = 0, \tag{2.5}$$

where the prime designates derivation with respect to the argument. Dividing all the terms in Equation (2.5) by $U(\rho)\Phi(\phi)/\rho^2$ and rearranging them yields

$$\frac{\rho^2 U''(\rho)}{U(\rho)} + \frac{\rho^2 U'(\rho)}{U(\rho)} + \chi^2\rho^2 = \frac{\Phi''(\phi)}{\Phi(\phi)}, \tag{2.6}$$

where the left-hand side of Equation (2.6) is only a function of ρ and right-hand side is only a function of ϕ. Since each side of Equation (2.6) is function of one variable exclusively, a solution may exist if and only if either side is equal to a constant. Separation constants must be negative, since azimuthally periodic solutions are looked for.

The azimuthal equation is written as

$$\Phi''(\phi) + q^2\Phi(\phi) = 0, \tag{2.7}$$

with $-q^2$ the separation constant. The solution of Equation (2.7) is

$$\begin{aligned}\Phi(\phi) &= \bar{C}e^{jq\phi} + \bar{D}e^{-jq\phi} \\ &= \bar{\bar{C}}\cos(q\phi) + \bar{\bar{D}}\sin(q\phi),\end{aligned} \tag{2.8}$$

where $\bar{C}$, $\bar{D}$, $\bar{\bar{C}}$, and $\bar{\bar{D}}$ are constant coefficients to be determined by the excitation.

The radial equation is multiplied by ρ^2 and rearranged to obtain the following form

$$U''(\rho) + \frac{1}{\rho}U'(\rho) + \left(\chi^2 + \frac{q^2}{\rho^2}\right)U(\rho) = 0. \tag{2.9}$$

Equation (2.9) is the modified version of Bessel differential equation and has the following solution

$$U(\rho) = \bar{A}J_q(\chi\rho) + \bar{B}Y_q(\chi\rho), \tag{2.10}$$

where $\bar{A}$ and $\bar{B}$ are constants, $J_q(\cdot)$ and $Y_q(\cdot)$ are respectively the ordinary Bessel functions of the first and second kind, and order q.

From Equations (2.8) and (2.10), the expression of the monochromatic Bessel beam of order q is thus given by

$$\Psi(\rho,\phi,z,t;\chi,q,\beta,\omega)=AJ_q(\chi\rho)e^{jq\phi}e^{-j\beta z}e^{j\omega t}, \tag{2.11}$$

where A is a constant amplitude, $Y_q(\chi\rho)$ is eliminated since it diverges as its argument goes to zero and thus, does not represent a physical solution. The exponential representation of the azimuthal dependence is chosen over the sinusoidal representation because solutions with rotating phase are sought. The expression in Equation (2.11) describes a monochromatic wave propagating in the $+z-$direction with a Bessel function of order q as its radial profile. The azimuthal (or angular) dependence determines the phase helicity and accordingly the OAM-state of the beam.

So far, only the scalar vortex beam solutions are discussed. Next, the electromagnetic vectorial vortex beams from the scalar solutions are derived. Hertz vector potentials are used to derive the electromagnetic Bessel solutions, and then construct vortex beams. The electric and magnetic fields are derived from the Hertz vector potentials as [44]

$$\mathbf{E}=\nabla(\nabla\cdot\Pi_e)-\frac{1}{c^2}\frac{\partial^2}{\partial t^2}\Pi_e-\mu_0\nabla\times\left(\frac{\partial}{\partial t}\Pi_h\right), \tag{2.12}$$

$$\mathbf{H}=\varepsilon_0\nabla\times\left(\frac{\partial}{\partial t}\Pi_e\right)+\nabla(\nabla\cdot\Pi_h)-\frac{1}{c^2}\frac{\partial^2}{\partial t^2}\Pi_h, \tag{2.13}$$

where ε_0 and μ_0 are the free-space permittivity and permeability, respectively, and Π_e and Π_h are the electric and magnetic Hertz vector potentials, which satisfy the source-free vector wave equation

$$\nabla\times\nabla\times\Pi(\mathbf{r},t)-\varepsilon_0\mu_0\frac{\partial^2}{\partial t^2}\Pi(\mathbf{r},t)=0. \tag{2.14}$$

Assuming the harmonic-time dependence $\exp(j\omega t)$, Equation (2.14) reduces to the vector Helmholtz equation

$$\nabla \times \nabla \times \Pi(\mathbf{r},\omega) + k^2 \Pi(\mathbf{r},\omega) = 0, \tag{2.15}$$

where $\omega^2 \varepsilon_0 \mu_0 = \omega^2 / c^2 = k^2$.

Next, Equation (2.15) is separated in transverse electric (TE) and transverse magnetic (TM) fields in the circular cylindrical coordinate system. TE and TM separation in this coordinate system requires that the Hertz vector potentials have a single component, namely in the $z-$direction [44]. This reduces Equation (2.15) to Equation (2.2), for which Bessel beam solution is already established. In such case, Π_e yields the TE field, whereas Π_h yields the TM field. Hence, the Hertz vector potentials are written as

$$\Pi_{e/h}(\mathbf{r},t) = A_{e/h} \Psi(\mathbf{r},t) \hat{\mathbf{z}}, \tag{2.16}$$

where Ψ is scalar Bessel function as given in Equation (2.11), $A_{e/h}$ is an arbitrary amplitude for the electric/magnetic Hertz vector potential component, and $\hat{\mathbf{z}}$ is the unit vector in the $z-$direction.

Next, TE and TM fields are derived in the circular cylindrical coordinate system from scalar Bessel beams. Substituting Equation (2.11) into Equation (2.16) and then into Equations (2.12) and (2.13) yields the TE vortex beam complex electric and magnetic fields as

$$
\begin{aligned}
E_\rho(\rho,\phi,z,t) &= -A_e \frac{q\mu_0 k}{\chi^2 \rho} e^{jq\phi} e^{-j[\beta z-\omega t]} J_q(\chi\rho), \\
E_\phi(\rho,\phi,z,t) &= A_e \frac{j\mu_0 k}{\chi^2} e^{jq\phi} e^{-j[\beta z-\omega t]} \frac{\partial}{\partial\rho} J_q(\chi\rho), \\
E_z(\rho,\phi,z,t) &= 0,
\end{aligned} \tag{2.17}
$$

$$
\begin{aligned}
H_\rho(\rho,\phi,z,t) &= -A_e \frac{j\beta}{\chi^2} e^{jq\phi} e^{-j[\beta z-\omega t]} \frac{\partial}{\partial\rho} J_q(\chi\rho), \\
H_\phi(\rho,\phi,z,t) &= -A_e \frac{q\beta}{\chi^2 \rho} e^{jq\phi} e^{-j[\beta z-\omega t]} J_q(\chi\rho), \\
H_z(\rho,\phi,z,t) &= A_e e^{jq\phi} e^{-j[\beta z-\omega t]} J_q(\chi\rho),
\end{aligned} \tag{2.18}
$$

and the TM vortex beam complex electric and magnetic fields as

$$
\begin{aligned}
E_\rho(\rho,\phi,z,t) &= -A_h \frac{j\beta}{\chi^2} e^{jq\phi} e^{-j[\beta z-\omega t]} \frac{\partial}{\partial\rho} J_q(\chi\rho), \\
E_\phi(\rho,\phi,z,t) &= -A_h \frac{q\beta}{\chi^2 \rho} e^{jq\phi} e^{-j[\beta z-\omega t]} J_q(\chi\rho), \\
E_z(\rho,\phi,z,t) &= A_h e^{jq\phi} e^{-j[\beta z-\omega t]} J_q(\chi\rho),
\end{aligned} \tag{2.19}
$$

$$
\begin{aligned}
H_\rho(\rho,\phi,z,t) &= -A_h \frac{q\varepsilon_0 k}{\chi^2 \rho} e^{jq\phi} e^{-j[\beta z-\omega t]} J_q(\chi\rho), \\
H_\phi(\rho,\phi,z,t) &= A_h \frac{j\varepsilon_0 k}{\chi^2} e^{jq\phi} e^{-j[\beta z-\omega t]} \frac{\partial}{\partial\rho} J_q(\chi\rho), \\
H_z(\rho,\phi,z,t) &= 0.
\end{aligned} \tag{2.20}
$$

Note that for vortex beams, the topological charge is non-zero ($q \neq 0$). Polarization of such higher order Bessel beams is always a combination of radial and azimuthal polarizations, while linear and elliptic polarizations are not possible. No transverse electromagnetic (TEM) Bessel beam solution exists either, since a Bessel beam is a superposition of plane-waves propagating oblique to the beam axis.

2.2.1 Vortex Beams in Optics

Scalar vortex beams used in optics are generally not of the Bessel type as derived in the previous section. More often than not, they are based on Laguerre-Gaussian modes. The beam profile is specified using generalized Laguerre polynomials [45]. In 1992, it was shown by Allen *et al.* that Gaussian modes can possess orbital angular momentum, more specifically, TEM_{plq} modes possess well-defined orbital angular momenta [46].

For practical laser fields it is sufficient to only consider quasi-monochromatic fields with a rather well-defined direction of propagation. It suffices to consider a beam of angular frequency ω propagating in the $z-$direction and the beam being linearly polarized, for the sake of simplicity [47]. The field spatial function, $\upsilon(\mathbf{r})$, satisfies the Helmholtz equation

$$\left[\nabla^2 + k^2\right]\upsilon(\mathbf{r}) = 0. \tag{2.21}$$

The paraxial wave equation is obtained with the ansatz

$$\upsilon = u(\mathbf{r})e^{-jkz}. \tag{2.22}$$

Substituting Equation (2.22) into Equation (2.21) yields

$$\nabla_\perp^2 u + \frac{\partial^2}{\partial z^2}u - 2jk\frac{\partial}{\partial z}u = 0. \tag{2.23}$$

The paraxial approximation requires that the variation of u in the $z-$direction is slow, which allows us to drop the second derivative with respect to z and so arrive at the paraxial wave equation

$$j\frac{\partial}{\partial z}u = \frac{1}{2k}\nabla_\perp^2 u, \tag{2.24}$$

which is formally equivalent to the Schrödinger equation in two dimensions.

Many solutions are known for the paraxial wave equation and most of them are used to describe laser fields, including Gaussian beams and the higher-order Hermite-Gaussian modes. Laguerre-Gaussian solutions are of interest, here. These are the most conveniently expressed in circular cylindrical coordinates and take the following form

$$u_{q,p}(\rho,\phi,z)=\sqrt{\frac{2p!}{\pi(p+|q|)!}}\frac{1}{w(z)}\left(\frac{\rho\sqrt{2}}{w(z)}\right)^{|q|}\exp\left(\frac{-\rho^2}{w^2(z)}\right)L_p^{|q|}\left(\frac{2\rho^2}{w^2(z)}\right)e^{jq\phi}$$
$$\times\exp\left(jk\frac{\rho^2 z}{2\left(z_R^2+z^2\right)}\right)\exp\left[j(2p+|q|+1)\tan^{-1}\left(\frac{z}{z_R}\right)\right], \tag{2.25}$$

where $L_p^{|q|}$ is the associated Laguerre polynomial, $z_R = kw^2(0)/2$ is the Rayleigh range (a measure of the tightness of the focus), design parameter $w(0)$ is the Gaussian beam waist, is the radius at which the intensity has decreased to $1/e^2$ or 0.135 of its peak value, and $w(z)=w(0)\sqrt{1+z^2/z_R^2}$ is the beam width. It is evident from equation (2.25) that the azimuthal dependence takes the form $\exp(jq\phi)$, which corresponds to the phase helicity of vortex beams. A wave function with this azimuthal phase dependence is an eigenstate of the orbital angular momentum operator

$$\hat{L}_z = -j\hbar\frac{\partial}{\partial\phi} \tag{2.26}$$

with $\hbar$ being Planck's constant, and having eigenvalues $q\hbar$. Each photon in a Laguerre-Gaussian laser beam of the form Equation (2.25) carries an orbital angular momentum of $q\hbar$ [47].

In the eikonal approximation, which is suitable for paraxial beams, the Poynting vector has the following form

$$\mathbf{S} \propto \mathrm{Im}\left\{\upsilon^{*}\nabla\upsilon\right\} \tag{2.27}$$

This expression embodies the idea that the phase fronts are locally plane in form and that the normal to these gives the local direction of propagation of the energy. The longitudinal and azimuthal Poynting vector components of the Laguerre-Gaussian beam may thus be expressed as

$$\begin{aligned} S_z &\approx k|u|^2, \\ S_\phi &\approx \frac{q}{\rho}|u|^2. \end{aligned} \tag{2.28}$$

The radial component is associated with the spreading of the beam spot. The momentum density of such a beam is $\mathbf{g} = \mathbf{S}/c^2$ and it follows that the density of the z component of the OAM is

$$L_z = \rho g_\phi = \frac{q|u|^2}{c^2}. \tag{2.29}$$

The local energy density is $\epsilon \approx c g_z$ so that

$$\frac{L_z}{\epsilon} = \frac{L}{\omega}. \tag{2.30}$$

The energy of a single photon is $\omega\hbar$ and it follows, therefore, that the orbital angular momentum is $q\hbar$ per photon.

2.3 Physics of Vortex Beams

So far, the field expressions for vector Bessel vortex beams and scalar Laguerre-Gaussian vortex beams are presented. In this section, the physical aspects pertaining to vortex beams, specifically in relation to their momenta, are covered.

Euler's laws of motion state that in order to fully and properly understand the motion of a system, one must consider both translational and rotational dynamics simultaneously. Euler's first law of motion concerns the translational dynamics and studies translational motion of objects and the effect of the forces on such motion. Linear momentum thus emerges as a defining attribute of translational dynamics, since the rate of change of linear momentum constitutes the force affecting translational motion. In electromagnetic field theory, linear momentum density is directly proportional to the Poynting vector and is to thank for existing radio information transfer. Euler's second law of motion concerns the rotational dynamics and studies torque action that causes angular acceleration of objects. Angular momentum thus emerges as a defining attribute of rotational dynamics, since the rate of change of angular momentum constitutes the torque affecting rotational motion. In electromagnetic field theory, angular momentum consists of: (i) spin angular momentum (SAM) which is responsible for the polarization of electromagnetic waves and has two eigenstates $\sigma = \pm 1$, and (ii) orbital angular momentum (OAM) which is responsible for the helicity (screw twist action) in the phase-front of the electromagnetic wave and has an infinite number of eigenstates $q = 0, \pm 1, \pm 2 \pm 3, \ldots$.

The Poynting vector prescribes the total energy transfer per unit area per unit time of an electromagnetic field and is defined in terms of fields as

$$\mathbf{S}(\mathbf{r},t)=\mathbf{E}(\mathbf{r},t)\times\mathbf{H}(\mathbf{r},t). \tag{2.31}$$

The linear momentum density of the wave can be expressed in terms of the Poynting vector as

$$\mathbf{p}(\mathbf{r},t)=\frac{1}{c^2}\mathbf{S}(\mathbf{r},t), \tag{2.32}$$

while the angular momentum density of the wave is expressed as

$$\mathbf{j}(\mathbf{r},t)=\mathbf{r}\times\mathbf{p}(\mathbf{r},t)=\frac{1}{c^2}\mathbf{r}\times\mathbf{S}(\mathbf{r},t). \tag{2.33}$$

Note that Equation (2.33) includes both SAM and OAM densities of the wave.

In the paraxial approximation, the local value of the linear momentum density is given by [48]

$$\mathbf{p}(\mathbf{r},t)=-j\omega\frac{\varepsilon_0}{2}\left(u^*\nabla u-u\nabla u^*\right)+\omega k\varepsilon_0|u|^2\hat{\mathbf{z}}+\omega\sigma\frac{\varepsilon_0}{2}\frac{\partial|u|^2}{\partial\rho}\boldsymbol{\phi}, \tag{2.34}$$

where $\hat{\mathbf{z}}$ and $\hat{\boldsymbol{\phi}}$ are unit vectors in the $z-$ and $\phi-$directions, respectively, σ is the polarization of the wave with $\sigma=+1$ corresponding to left-hand circular polarization, $\sigma=-1$ corresponding to right-hand circular polarization, and $\sigma=0$ corresponding to linear polarization.

The cross product of Equation (2.34) with the $\mathbf{r}$ gives the angular momentum density. In particular, an angular momentum density component in the $z-$direction, the direction of wave propagation, is directly proportional to the third term on the right-hand side of Equation (2.34), which is polarization dependent, but independent of the azimuthal phase. This suggests that this component gives rise to the SAM part of the angular momentum density vector. On the other hand, the first term on the right-hand side of Equation (2.34) is dependent on the phase gradient, but not the

polarization. This suggests that it gives rise to the OAM part of the angular momentum density vector.

For example, if u is taken as a circularly polarized Laguerre-Gaussian mode function as defined in Equation (2.25), the total local angular momentum density in the direction of propagation may be evaluated as

$$j_z = \varepsilon_0 \left[\omega q |u|^2 - \frac{1}{2} \omega \sigma \rho \frac{\partial |u|^2}{\partial \rho} \right]. \tag{2.35}$$

The total angular momentum of the wave is thus

$$J_z = (q + \sigma)\hbar, \tag{2.36}$$

with $\sigma\hbar$ SAM and $q\hbar$ OAM per photon.

It is worthwhile noting that SAM does not depend on the choice of a specific axis and hence is said to be "intrinsic". However, the angular momentum which results from p_z is said to be "extrinsic", because its value depends on the choice of the axis about which the momentum is calculated.

CHAPTER 3

LAUNCHER DESIGN

3.1 Introduction

In this chapter, the specifics of the launcher design are explained and a detailed modal analysis is performed to obtain field expressions generated by the launcher. The power in each excited mode is calculated using the derived modal expansion coefficients. Then, generated electric and magnetic fields are calculated through modal expansion coefficients as sum of waveguide modes.

3.2 Launcher Characteristics

The aim of the launcher is to generate vector vortex beams in the microwave regime based on waveguide modes, where the vortex beam is set to be the aperture field at the open-end of a metallic circular waveguide section. For simplicity and without loss of generality, a transverse electric (TE) beam with a truncated Bessel profile is considered. The aperture field is formed by the propagating field of the TE_{q1} mode of the waveguide, where q is the topological charge of vortex beam to be launched. Excitation is provided by means of a single circular loop antenna inserted coaxially inside the waveguide. In this design, the waveguide housing the large loop antenna is shown to be advantageous in terms of matching because the antenna input impedance depends on the antenna location inside the waveguide.

The design method takes inspiration from previous work on zero-order Bessel beam generation in the microwave regime [44], but accounts for the practical aspects,

namely, that the current on the antenna is not constant and that the antenna input impedance is matched to the source. Additionally, this method permits reducing the number of required antennas to a single antenna.

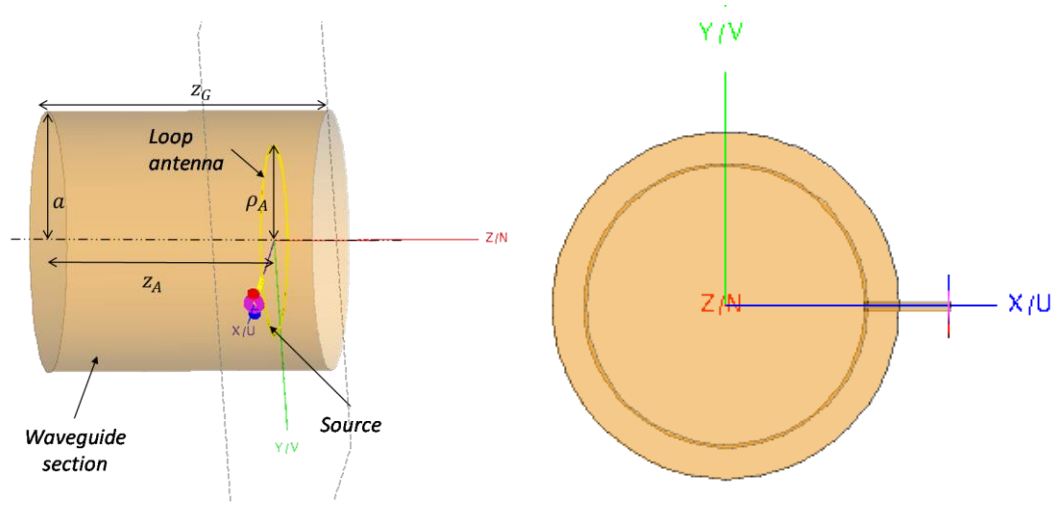

(a) **(b)**

Figure 3.1 (a) Schematic of the vortex beam launcher. The launcher consists of a circular waveguide section with a coaxially-aligned loop antenna. **(b)** Top view of the launcher structure.

The structure of the launcher consists of two main components: (i) a thin sheet loop antenna connected to a voltage source with $50\,\Omega$ resistance and (ii) a finite circular waveguide section with one closed end. The antenna and waveguide are coaxially aligned with the $z-$axis, as illustrated in Figure 3.1. The radius of the waveguide a is chosen such that

$$p'_{q1} < ak < p_{q1}, \tag{3.1}$$

where $k = 2\pi/\lambda$ is the free-space wavenumber and p_{q1} and p'_{q1} are the first roots of the $q-$th order Bessel function of the first kind and its derivative, respectively. This particular choice of a ensures that the TE_{q1} mode is propagating, while the next

mode with the same azimuthal dependence, the transverse magnetic TM_{q1} mode, is in cut-off. The radius of the loop antenna ρ_A is chosen such that the circumference length corresponds to $q\lambda$. This choice of circumference length together with the choice of the waveguide radius ensure that the antenna excites the TE_{q1} mode of the circular waveguide section, which is launched into free-space through the open-end.

The transverse profile of the launched vortex beam has a 'doughnut-shape' because the radial dependence of the TE_{q1} field corresponds to $q-$th order Bessel function truncated at its first zero. The distance of the antenna from the closed-end z_A is determined by the choice of q to maximize the power coupling efficiency to the TE_{q1} mode. Effect of the length of the waveguide section z_G on the overall performance of the launcher is studied in Chapter 4, in detail. As a rule of thumb, it is shown that the effect of z_G is minimal as long as, roughly speaking $z_G \geq 0.75\lambda_{g,q1}$, where $\lambda_{g,q1}$ is the wavelength of the launched mode inside the waveguide and is equal to $2\pi / \beta_{q1}^{\mathrm{TE}}$ and β_{q1}^{TE} is the propagation constant of the TE_{q1} mode.

3.3 Modal Analysis

Modal analysis is carried out on the field excited by the loop antenna in order to understand the behavior of the launcher. The modal analysis achieves two main goals: (i) verify the soundness of the design and to demonstrate that the launcher indeed generates the required vortex beam, (ii) give a wide perspective on how the launcher design may be modified to fulfill other requirements, thus providing an

insight on performance bounds of this specific design and all similar designs based on the same concept.

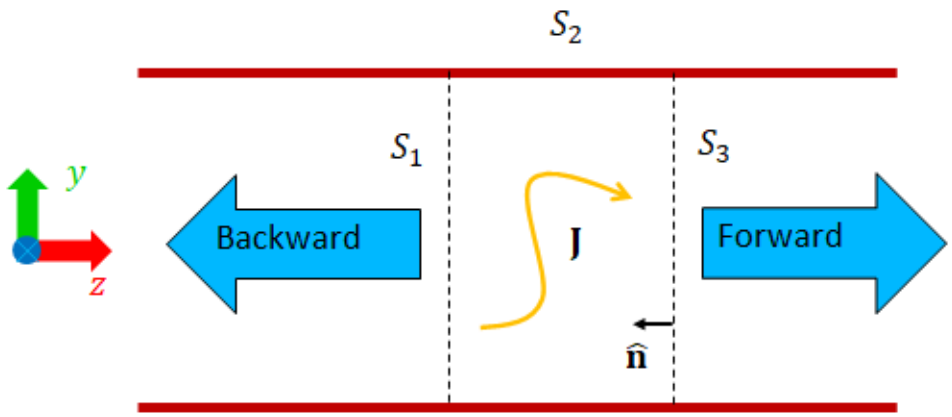

Figure 3.2 An illustration of a waveguide with a current filament source. The source region is marked with vertical dashed lines and the arrows indicate the direction of propagation (or decay) of the excited fields.

For the sake of analysis simplicity, an infinite circular waveguide with an arbitrary current source $\mathbf{J}$ located inside the waveguide is assumed, as illustrated in Figure 3.2. The source region is indicated by the dashed lines in Figure 3.2 and is imagined as a cylinder with the dashed lines indicting its top and bottom circular faces. Outside of the source region, the fields propagate or decay away from the source. On the left hand side, the fields generated by the source are backward-propagating (or decaying if they are evanescent waves) and on the right hand side they are forward-propagating/decaying. The excited field due to a current source $\mathbf{J}(\rho,\phi,z)$ may be expressed as superposition of the circular waveguide eigenmodes, such as [49]

$$
\begin{aligned}
\mathbf{E}^{+} &= \sum_{\nu} a_{\nu}\mathbf{E}_{\nu}^{+}, \\
\mathbf{H}^{+} &= \sum_{\nu} a_{\nu}\mathbf{H}_{\nu}^{+}, \\
\mathbf{E}^{-} &= \sum_{\nu} b_{\nu}\mathbf{E}_{\nu}^{-}, \\
\mathbf{H}^{-} &= \sum_{\nu} b_{\nu}\mathbf{H}_{\nu}^{-},
\end{aligned}
\tag{3.2}
$$

where $\mathbf{E}$ and $\mathbf{H}$ are the electric and magnetic fields, respectively, subscripts $\pm$ designate fields radiating or decaying in the $\pm z-$direction, respectively, ν is a generic index for a waveguide mode, and a_{ν} and b_{ν} are excitation coefficients to be determined.

Mode field expressions on the right-hand side of Equation (3.2) can be represented in terms of transverse field components ($\mathbf{e}_{\nu}$ and $\mathbf{h}_{\nu}$) and longitudinal field components ($\mathrm{e}_{z\nu}$ and $\mathrm{h}_{z\nu}$) as follows

$$
\begin{aligned}
\mathbf{E}_{\nu}^{+} &= \left[\mathbf{e}_{\nu} + \mathrm{e}_{z\nu}\hat{\boldsymbol{z}}\right]e^{-\gamma_{\nu}z}, \\
\mathbf{H}_{\nu}^{+} &= \left[\mathbf{h}_{\nu} + \mathrm{h}_{z\nu}\hat{\boldsymbol{z}}\right]e^{-\gamma_{\nu}z}, \\
\mathbf{E}_{\nu}^{-} &= \left[\mathbf{e}_{\nu} - \mathrm{e}_{z\nu}\hat{\boldsymbol{z}}\right]e^{+\gamma_{\nu}z}, \\
\mathbf{H}_{\nu}^{-} &= \left[-\mathbf{h}_{\nu} + \mathrm{h}_{z\nu}\hat{\boldsymbol{z}}\right]e^{+\gamma_{\nu}z},
\end{aligned}
\tag{3.3}
$$

where γ_{ν} is the propagation constant of the ν mode.

Maxwell's equations with the source term $\mathbf{J}$ can be written as follows to describe the fields generated by that source

$$
\begin{aligned}
\nabla\times\mathbf{E} &= -j\omega\mu_0\mathbf{H}, \\
\nabla\times\mathbf{H} &= j\omega\varepsilon_0\mathbf{E} + \mathbf{J}.
\end{aligned}
\tag{3.4}
$$

In a source-free waveguide, Maxwell's equations apply to the waveguide modes as

$$\nabla \times \mathbf{E}_\nu^\pm = -j\omega\mu_0 \mathbf{H}_\nu^\pm,$$
$$\nabla \times \mathbf{H}_\nu^\pm = j\omega\varepsilon_0 \mathbf{E}_\nu^\pm. \tag{3.5}$$

In order to establish the relationship between the fields and the source in the source region and the waveguide modes to determine the modal excitation coefficients, Lorentz reciprocity principle is used, which reads

$$\oiint_S \left[\mathbf{E}_1 \times \mathbf{H}_2 - \mathbf{E}_2 \times \mathbf{H}_1\right] \cdot \hat{\mathbf{n}} dS = \iiint_V \left[\mathbf{J}_1 \cdot \mathbf{E}_2 - \mathbf{J}_2 \cdot \mathbf{E}_1\right] dV, \tag{3.6}$$

where $\mathbf{E}_{1,2}$ and $\mathbf{H}_{1,2}$ are, respectively, the electric and magnetic fields excited by the currents $\mathbf{J}_{1,2}$, V is a volume enclosing the sources, and S is the surface of V.

In order to apply Lorentz reciprocity, equations (3.4) and (3.5) are respectively multiplied by the mode fields and the source fields, viz.

$$\mathbf{H}_\nu^\pm \cdot \nabla \times \mathbf{E} = -j\omega\mu_0 \mathbf{H} \cdot \mathbf{H}_\nu^\pm,$$
$$\mathbf{E}_\nu^\pm \cdot \nabla \times \mathbf{H} = j\omega\varepsilon_0 \mathbf{E} \cdot \mathbf{E}_\nu^\pm + \mathbf{J} \cdot \mathbf{E}_\nu^\pm, \tag{3.7}$$

$$\mathbf{H} \cdot \nabla \times \mathbf{E}_\nu^\pm = -j\omega\mu_0 \mathbf{H}_\nu^\pm \cdot \mathbf{H},$$
$$\mathbf{E} \cdot \nabla \times \mathbf{H}_\nu^\pm = j\omega\varepsilon_0 \mathbf{E}_\nu^\pm \cdot \mathbf{E}, \tag{3.8}$$

and then subtract the sum of the source region in Equation (3.7) from the sum of the source-free region in Equation (3.8), which yields an expression dependent on the source and waveguide modes ($-\mathbf{J} \cdot \mathbf{E}_\nu^\pm$) as follows

$$\mathbf{H} \cdot \nabla \times \mathbf{E}_\nu^\pm - \mathbf{E}_\nu^\pm \cdot \nabla \times \mathbf{H} - \mathbf{H}_\nu^\pm \cdot \nabla \times \mathbf{E} + \mathbf{E} \cdot \nabla \times \mathbf{H}_\nu^\pm = -\mathbf{J} \cdot \mathbf{E}_\nu^\pm, \tag{3.9}$$

and using the vector identity

$$\mathbf{Y} \cdot \nabla \times \mathbf{X} - \mathbf{X} \cdot \nabla \times \mathbf{Y} = \nabla \cdot \left(\mathbf{X} \times \mathbf{Y}\right), \tag{3.10}$$

the expression in equation (3.9) is further simplified to

$$\nabla \cdot \left(\mathbf{E}_{\nu}^{\pm} \times \mathbf{H} - \mathbf{E} \times \mathbf{H}_{\nu}^{\pm} \right) = -\mathbf{J} \cdot \mathbf{E}_{\nu}^{\pm}. \tag{3.11}$$

Next, Equation (3.11) is integrated over a volume enclosing the source region

$$\iiint_V \nabla \cdot \left(\mathbf{E}_{\nu}^{\pm} \times \mathbf{H} - \mathbf{E} \times \mathbf{H}_{\nu}^{\pm} \right) = \iiint_V -\mathbf{J} \cdot \mathbf{E}_{\nu}^{\pm}, \tag{3.12}$$

and applying the divergence theorem

$$\iiint_V \nabla \cdot \mathbf{X} dV = -\oiint_S \mathbf{X} \cdot \hat{\mathbf{n}} dS, \tag{3.13}$$

to the left-hand side of Equation (3.12) to establish the relation between the source current and the excited waveguide modes. In Equation (3.13), $\mathbf{n}$ is unit normal vector to S, and it is selected in the inward direction to simplify the expression as

$$\oiint_S \left(\mathbf{E}_{\nu}^{\pm} \times \mathbf{H} - \mathbf{E} \times \mathbf{H}_{\nu}^{\pm} \right) \cdot \hat{\mathbf{n}} dS = \iiint_V \mathbf{J} \cdot \mathbf{E}_{\nu}^{\pm} dV. \tag{3.14}$$

The closed surface S is composed of three surfaces enclosing the source region, as illustrated in Figure 3.2. S_1 and S_3 are the top and bottom surfaces of the cylinder, and S_2 is the side of the cylinder. The integral over S_2 identically vanishes because of the boundary condition that dictates that the tangential electric field vanishes at a perfect electric conductor (PEC) boundary.

3.3.1 Waveguide Modes and Orthogonality Relation

To determine the excitation coefficients of the waveguide modes, the mode orthogonality relation is employed. To this end, the field expressions in Equation (3.2) are inserted into Equation (3.14) yielding

$$\begin{aligned} \oiint_{S_1} \left(\mathbf{E}_{\mu}^{\pm} \times \sum_{\nu} b_{\nu} \mathbf{H}_{\nu}^{-} - \sum_{\nu} b_{\nu} \mathbf{E}_{\nu}^{-} \times \mathbf{H}_{\mu}^{\pm} \right) \cdot \hat{\mathbf{n}} dS &= \iiint_V \mathbf{J} \cdot \mathbf{E}_{\mu}^{\pm} dV, \\ \oiint_{S_3} \left(\mathbf{E}_{\mu}^{\pm} \times \sum_{\nu} a_{\nu} \mathbf{H}_{\nu}^{+} - \sum_{\nu} a_{\nu} \mathbf{E}_{\nu}^{+} \times \mathbf{H}_{\mu}^{\pm} \right) \cdot \hat{\mathbf{n}} dS &= \iiint_V \mathbf{J} \cdot \mathbf{E}_{\mu}^{\pm} dV. \end{aligned} \tag{3.15}$$

Next, the mode orthonormality relation

$$\iint_S \left(\mathbf{e}_\nu \times \mathbf{h}_\mu\right) \cdot \hat{\mathbf{n}} dS = \delta_{\nu\mu}, \tag{3.16}$$

where $\delta_{\nu\mu}$ is Kronecker delta which is equal to 1 if $\nu = \mu$ and 0 elsewhere, is applied to Equation (3.15). By taking advantage of Equation (3.3) and retaining only the transverse field components, the left-hand side integral at S_1 reduces to

$$\begin{gathered} \iint_{S_1} \left(\mathbf{e}_\mu \times \left(-b_\nu \mathbf{h}_\nu\right) - b_\nu \mathbf{e}_\nu \times \mathbf{h}_\mu\right) \cdot \hat{\mathbf{z}} dS = -2b_\nu, \\ \iint_{S_1} \left(\mathbf{e}_\mu \times \left(-b_\nu \mathbf{h}_\nu\right) - b_\nu \mathbf{e}_\nu \times \left(-\mathbf{h}_\mu\right)\right) \cdot \hat{\mathbf{z}} dS = 0. \end{gathered} \tag{3.17}$$

Similarly at S_3, the left-hand side integral in equation (3.15) reduces to

$$\begin{gathered} \iint_{S_3} \left(\mathbf{e}_\mu \times \left(a_\nu \mathbf{h}_\nu\right) - a_\nu \mathbf{e}_\nu \times \mathbf{h}_\mu\right) \cdot \left(-\hat{\mathbf{z}}\right) dS = 0, \\ \iint_{S_3} \left(\mathbf{e}_\mu \times \left(a_\nu \mathbf{h}_\nu\right) - a_\nu \mathbf{e}_\nu \times \left(-\mathbf{h}_\mu\right)\right) \cdot \left(-\hat{\mathbf{z}}\right) dS = -2a_\nu. \end{gathered} \tag{3.18}$$

3.3.2 Mode Excitation Coefficients

Using the two non-zero integrals at S_1 and S_3 given in Equations (3.17) and (3.18), Lorentz reciprocity principle for forward propagating modes yields

$$-2b_\nu = \iiint_V \mathbf{J} \cdot \mathbf{E}_\nu^+ dV, \tag{3.19}$$

and similarly for backward propagating modes

$$-2a_\nu = \iiint_V \mathbf{J} \cdot \mathbf{E}_\nu^- dV. \tag{3.20}$$

Equations (3.19) and (3.20) give the sought after modal excitation coefficients in terms of the source current as follows

$$a_\nu = -\frac{1}{2}\iiint_V \mathbf{J}\cdot\mathbf{E}_\nu^- dV,$$
$$b_\nu = -\frac{1}{2}\iiint_V \mathbf{J}\cdot\mathbf{E}_\nu^+ dV. \tag{3.21}$$

For the proposed launcher, the current is assumed to exist as a circular filament located at $z = z_A$ and $\rho = \rho_A$ and is non-uniform in the angular direction. The waveguide section is assumed to be infinite for the sake of insight; however modification for the actual waveguide section is straightforward by taking the reflections from waveguide ends into account. Hence, the current density on the loop antenna is modeled as

$$\mathbf{J}(\rho,\phi,z) = Ae^{-jq\phi}\delta(z-z_A)\frac{\delta(\rho-\rho_A)}{\rho}\hat{\boldsymbol{\phi}}, \tag{3.22}$$

where A is an arbitrary excitation amplitude, $\delta(\cdot)$ is the Dirac delta function, and $\hat{\boldsymbol{\phi}}$ is the unit vector in the $\phi-$direction. Substituting Equation (3.22) into Equation (3.21) yields

$$a_\nu = -\frac{A}{2}\int_{-\infty}^{\infty}\int_{-\pi}^{\pi}\int_0^a \frac{\delta(z-z_A)\delta(\rho-\rho_A)}{\rho}e^{-jq\phi}\hat{\boldsymbol{\phi}}\cdot\mathbf{E}_\nu^-\rho d\rho d\phi dz,$$
$$b_\nu = -\frac{A}{2}\int_{-\infty}^{\infty}\int_{-\pi}^{\pi}\int_0^a \frac{\delta(z-z_A)\delta(\rho-\rho_A)}{\rho}e^{-jq\phi}\hat{\boldsymbol{\phi}}\cdot\mathbf{E}_\nu^+\rho d\rho d\phi dz. \tag{3.23}$$

Next, the waveguide modes are expressed in their transverse and longitudinal components, as

$$\mathbf{E}_\nu^+(\rho,\phi,z) = \left[\mathrm{e}_{\rho\nu}(\rho,\phi)\hat{\boldsymbol{\rho}} + \mathrm{e}_{\phi\nu}(\rho,\phi)\hat{\boldsymbol{\phi}} + \mathrm{e}_{z\nu}(\rho,\phi)\hat{\mathbf{z}}\right]e^{-\gamma_\nu z},$$
$$\mathbf{E}_\nu^-(\rho,\phi,z) = \left[\mathrm{e}_{\rho\nu}(\rho,\phi)\hat{\boldsymbol{\rho}} + \mathrm{e}_{\phi\nu}(\rho,\phi)\hat{\boldsymbol{\phi}} - \mathrm{e}_{z\nu}(\rho,\phi)\hat{\mathbf{z}}\right]e^{\gamma_\nu z}, \tag{3.24}$$

where the dot-product selects only the $\mathrm{e}_{\phi\nu}$ component and the Dirac delta functions replace every z and ρ in the expression by z_A and ρ_A, respectively, which results in the following expressions

$$\begin{aligned} a_\nu &= -\frac{A}{2} e^{\gamma_\nu z_A} \int_{-\pi}^{\pi} e^{-jq\phi} \mathrm{e}_{\phi\nu}\left(\rho_A, \phi\right) d\phi, \\ b_\nu &= -\frac{A}{2} e^{-\gamma_\nu z_A} \int_{-\pi}^{\pi} e^{-jq\phi} \mathrm{e}_{\phi\nu}\left(\rho_A, \phi\right) d\phi. \end{aligned} \tag{3.25}$$

The field component $\mathrm{e}_{\phi\nu}$ may now be expressed in terms of the waveguide TE and TM modes, $\mathrm{e}_\phi^{\mathrm{TE}}$ and $\mathrm{e}_\phi^{\mathrm{TM}}$, as [50]

$$\begin{aligned} \mathrm{e}_{\phi nm}^{\mathrm{TE}}\left(\rho, \phi\right) &= \frac{j\omega\mu_0}{k_{c_{nm}}^{\mathrm{TE}}} \left[e^{jn\phi} + e^{-jn\phi} \right] J'_n\left(k_{c_{nm}}^{\mathrm{TE}} \rho\right), \\ \mathrm{e}_{\phi nm}^{\mathrm{TM}}\left(\rho, \phi\right) &= \frac{j\gamma_{nm}^{\mathrm{TM}} n}{\left(k_{c_{nm}}^{\mathrm{TM}}\right)^2 \rho} \left[e^{jn\phi} - e^{-jn\phi} \right] J_n\left(k_{c_{nm}}^{\mathrm{TM}} \rho\right), \end{aligned} \tag{3.26}$$

where $J_n(\cdot)$ and $J'_n(\cdot)$ are the n-th order Bessel function of the first kind and its derivative, respectively, $k_{c_{nm}}^{\mathrm{TE}} = p'_{nm} / a$ and $k_{c_{nm}}^{\mathrm{TM}} = p_{nm} / a$ are the TE and TM mode transverse wavenumbers, respectively, and $\gamma_{nm}^2 = k_0^2 - k_{c_{nm}}^2$. Substituting Equation (3.26) into Equation (3.25) yields

$$\begin{aligned} a_{nm}^{\mathrm{TE}} &= -\frac{A}{2} \frac{j\omega\mu_0}{k_{c_{nm}}^{\mathrm{TE}}} J'_n\left(k_{c_{nm}}^{\mathrm{TE}} \rho_A\right) e^{\gamma_{nm}^{\mathrm{TE}} z_A} \int_{-\pi}^{\pi} e^{-jq\phi} \left[e^{jn\phi} + e^{-jn\phi} \right] d\phi, \\ a_{nm}^{\mathrm{TM}} &= \frac{A}{2} \frac{j\gamma_{nm}^{\mathrm{TM}} n}{\left(k_{c_{nm}}^{\mathrm{TM}}\right)^2 \rho_A} J_n\left(k_{c_{nm}}^{\mathrm{TM}} \rho_A\right) e^{\gamma_{nm}^{\mathrm{TM}} z_A} \int_{-\pi}^{\pi} e^{-jq\phi} \left[e^{jn\phi} - e^{-jn\phi} \right] d\phi, \\ b_{nm}^{\mathrm{TE}} &= -\frac{A}{2} \frac{j\omega\mu_0}{k_{c_{nm}}^{\mathrm{TE}}} J'_n\left(k_{c_{nm}}^{\mathrm{TE}} \rho_A\right) e^{-\gamma_{nm}^{\mathrm{TE}} z_A} \int_{-\pi}^{\pi} e^{-jq\phi} \left[e^{jn\phi} + e^{-jn\phi} \right] d\phi, \\ b_{nm}^{\mathrm{TM}} &= \frac{A}{2} \frac{j\gamma_{nm}^{\mathrm{TM}} n}{\left(k_{c_{nm}}^{\mathrm{TM}}\right)^2 \rho_A} J_n\left(k_{c_{nm}}^{\mathrm{TM}} \rho_A\right) e^{-\gamma_{nm}^{\mathrm{TM}} z_A} \int_{-\pi}^{\pi} e^{-jq\phi} \left[e^{jn\phi} - e^{-jn\phi} \right] d\phi. \end{aligned} \tag{3.27}$$

Using the orthogonality relation of exponential functions

$$\int_{-\pi}^{\pi} e^{jn\phi} e^{-jm\phi} d\phi = 2\pi\delta_{nm}, \tag{3.28}$$

the modal excitation coefficients for TE and TM modes are found as

$$\begin{aligned}
a_{nm}^{\mathrm{TE}} &= -A\pi e^{\gamma_{nm}^{\mathrm{TE}} z_A} \frac{j\omega\mu_0}{k_{c_{nm}}^{\mathrm{TE}}} J'_n\left(k_{c_{nm}}^{\mathrm{TE}} \rho_A\right)\delta_{nq}, \\
a_{nm}^{\mathrm{TM}} &= -A\pi e^{\gamma_{nm}^{\mathrm{TM}} z_A} \frac{j\gamma_{nm}^{\mathrm{TM}} n}{\left(k_{c_{nm}}^{\mathrm{TM}}\right)^2 \rho_A} J_n\left(k_{c_{nm}}^{\mathrm{TM}} \rho_A\right)\delta_{nq}, \\
b_{nm}^{\mathrm{TE}} &= -A\pi e^{-\gamma_{nm}^{\mathrm{TE}} z_A} \frac{j\omega\mu_0}{k_{c_{nm}}^{\mathrm{TE}}} J'_n\left(k_{c_{nm}}^{\mathrm{TE}} \rho_A\right)\delta_{nq}, \\
b_{nm}^{\mathrm{TM}} &= A\pi e^{-\gamma_{nm}^{\mathrm{TM}} z_A} \frac{j\gamma_{nm}^{\mathrm{TM}} n}{\left(k_{c_{nm}}^{\mathrm{TM}}\right)^2 \rho_A} J_n\left(k_{c_{nm}}^{\mathrm{TM}} \rho_A\right)\delta_{nq}.
\end{aligned} \tag{3.29}$$

As the Kronecker delta functions in Equation (3.29) imply, the coefficients are non-zero only when $n = q$, hence it is evident that only TE_{qm} and TM_{qm} modes may be excited by the loop antenna current. Furthermore, the choice of a according to Equation (3.1) ensures that TE_{q1} is the only propagating mode inside the waveguide, as required by the design.

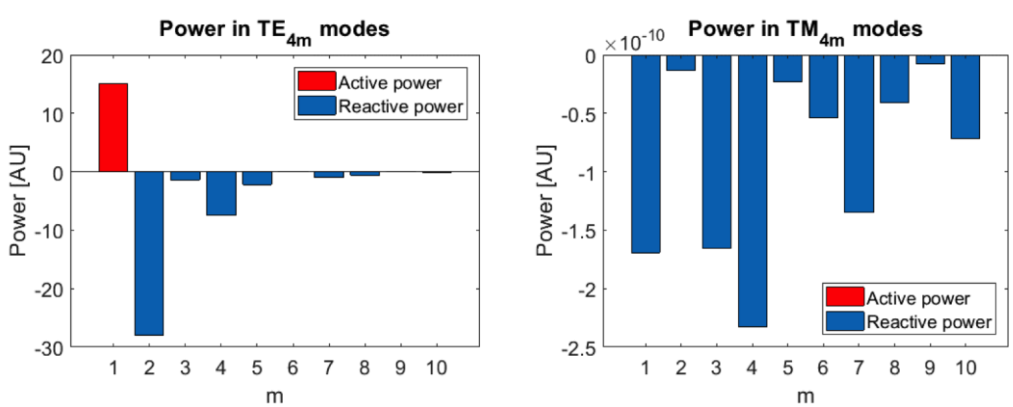

(a) **(b)**

Figure 3.3 (a) Active and reactive power in excited TE_{4m} modes. Note that only the TE_{41} is propagating as intended by the design. **(b)** Active and reactive power in TM_{4m} modes. Note that all TM modes are evanescent.

Using the excitation coefficients, the power distribution in different waveguide modes are computed for $q = 4$, as illustrated in Figure 3.3. Since only the TE_{41} mode is propagating, it is the only mode with active power, while all other modes carry reactive power. It is also observed that by using a loop antenna, the excited modes are almost exclusively TE_{4m} modes because the power stored in TM_{4m} modes is negligible compared to the power stored in TE_{4m} $(m \neq 1)$ modes. Additionally, it seems that a higher efficiency may be achieved by exciting TE_{42} for this structure. This would be true if the structure was indeed an infinite waveguide, however, due to the finiteness and the termination of the launcher, the efficiency is significantly increased employing the impedance matching techniques detailed in Chapter 4.

3.4 Generated Fields

3.4.1 Near Field

The electromagnetic performance of the launcher design is evaluated through full-wave simulations using multi-level fast multipole method (MLFMM) in Altair FEKO environment [51].

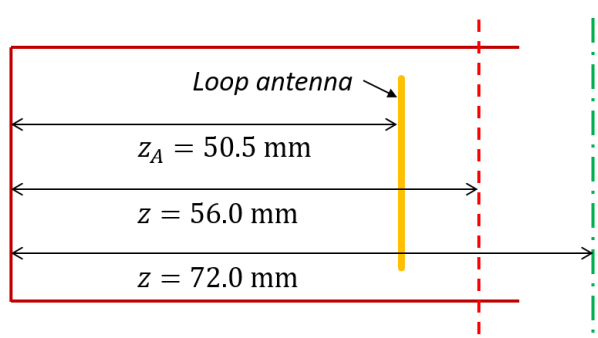

(a)

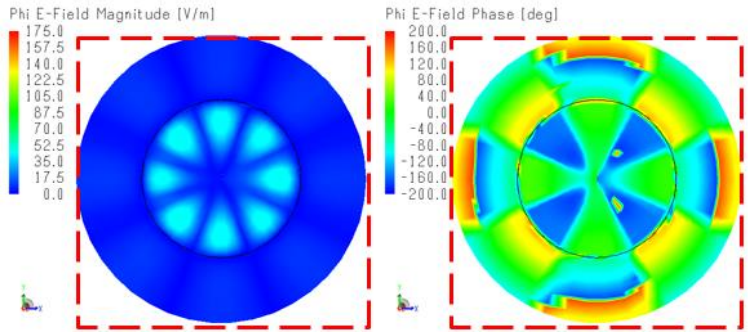

(b) **(c)**

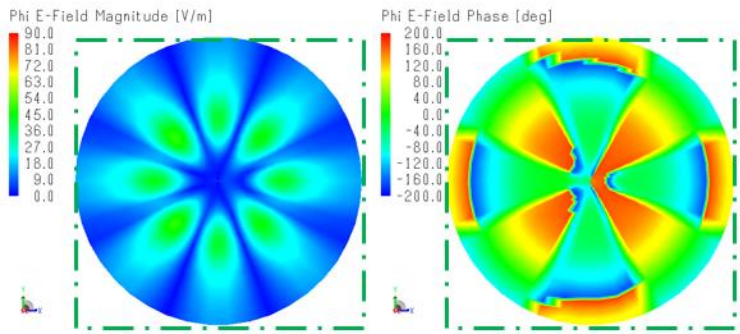

(d) **(e)**

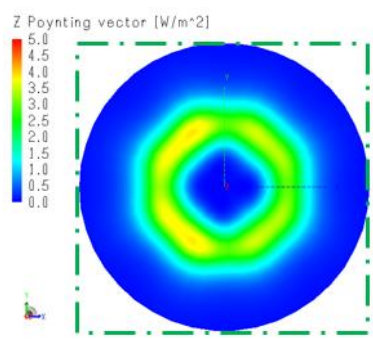

(f)

Figure 3.4 Plots of the electric field at different $z-$planes as shown in the schematic in **(a).** The **(b)** magnitude and **(c)** phase of E_ϕ at $z = 56\,\text{mm}$ inside the launcher, and the corresponding **(d)** magnitude and **(e)** phase at $z = 72\,\text{mm}$ in free-space. The phase plots show a helicity pertaining to $q = 4$ topological charge. The $z-$directed component of the Poynting vector is plotted at $z = 72\,\text{mm}$ in free-space in **(f)** and exhibits the expected 'doughnut-shape' profile.

Figure 3.4(a) shows a schematic of the measurement points with respect to antenna location. Figures 3.4(b) and 3.4(c), respectively, plot the magnitude and phase of the azimuthal component of the electric field E_ϕ at $z = 56\ \text{mm}$ inside the launcher structure. Figures 3.4(d) and 3.4(e), respectively, plot the corresponding values for the launched beam at $z = 72\ \text{mm}$ in free-space outside the launcher. In both cases, the phase exhibits the expected helicity pertaining to the $q = 4$ topological charge, while the magnitude displays a hollow center due to the phase discontinuity. The $z-$directed component of the Poynting vector, plotted in Figure 3.4(f), clearly shows the 'doughnut-shape' beam profile due to truncation of the Bessel function at its first zero. The full-wave simulation thus verifies that the proposed launcher is indeed capable of launching truncated vector Bessel beams carrying OAM with topological charge $q = 4$.

3.4.2 Far Field

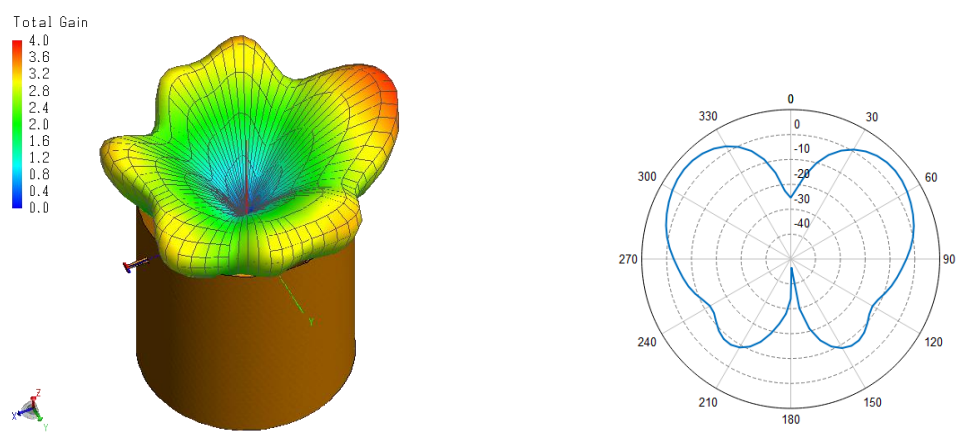

(a) **(b)**

Figure 3.5 Plots of the far-field radiation pattern **(a)** Conical radiation pattern of the launched vortex beam by the excited TE_{41} waveguide mode. The imperfect conical shape is due to the launcher's geometric asymmetry introduced by the voltage source feed line. **(b)** Polar plot of the gain pattern over wrapped $\theta-$plane at $\phi = 0^\circ$.

Figure 3.5(a) plots the far-field radiation pattern of the launcher in 3D. The pattern exhibits a clear null along the beam axis as expected. The imperfect conical shape is due to the asymmetry of the launcher geometry introduced by the feed line connecting the antenna to the source. Figure 3.5(b) plots the gain pattern of the launcher in polar format on wrapped $\theta-$plane at $\phi = 0^{\circ}$. Maximum gain occurs at $\theta = 45^{\circ}$ which shows the directive nature of the launcher. Further studies on directivity of the launcher are carried out in Chapter 4.

CHAPTER 4

PRACTICAL ASPECTS

4.1 Impedance Matching

In this section, the problem of impedance matching of a large loop antenna inside a circular waveguide section with a closed end is studied. Large loop antennas are not commonly used in free-space wireless applications due to their high radiation resistance and high input reactance, which make them difficult to match and, accordingly, operate at low radiation efficiency [52].

In this design, which is detailed in Chapter 3 and illustrated in Figure 3.1, the waveguide housing the large loop antenna is sought to be advantageous in terms of matching because the antenna input impedance changes with the antenna location inside the waveguide. The necessary conditions for single TE_{41} mode operation determine the value of the loop antenna radius ρ_A and set upper and lower bounds for the value of the waveguide radius a. The remaining design parameters, namely, the distance between the antenna and the closed-end of the waveguide section z_A and the total length of the waveguide section z_G are determined by the necessary conditions to optimally match the loop antenna to the voltage source with $50\,\Omega$ internal impedance.

In what follows, a method to construct the field-based antenna impedance model using the modal excitation coefficients derived in Chapter 3 is outlined. Next, an alternative simplified approach based on transmission line (TL) theory is detailed,

which is sought to be more useful due to its lower computational complexity and better physical insight.

4.1.1 Field-Based Input Impedance Model

In 1932, Carter came up with a way to compute the antenna impedance using Ohm's law [53]. If the voltage across the antenna's terminals and the current passing through those terminals are known, then the input impedance is determined in a straightforward fashion.

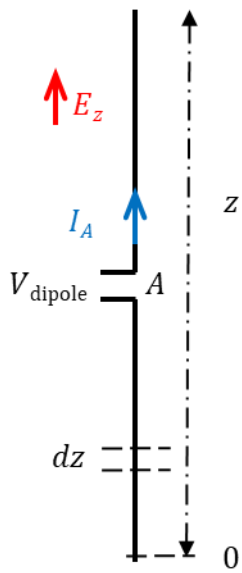

Figure 4.1 Schematic of a linear radiator as the basis of Carter's model.

In Carter's analysis, a dipole antenna of length l is used as illustrated in Figure 4.1, where a current with amplitude I_A varies sinusoidally along the antenna. To compute the terminal voltage, the electric field parallel to the antenna, E_z is such that

$$\frac{E_z dz}{I_A} = \frac{dV_{\text{dipole}}}{I_A \sin(kz)}. \tag{4.1}$$

Hence, the voltage difference across the antenna terminals V_{dipole} is found as

$$V_{\text{dipole}} = \int_0^l E_z \sin(kz)\, dz. \tag{4.2}$$

The antenna impedance hence can be expressed as

$$Z_{in,\text{dipole}} = \frac{V_{\text{dipole}}}{I_A}. \tag{4.3}$$

The same approach may be applied to the launcher as the excited fields are known through modal analysis. The voltage difference across the loop antenna input terminals is determined by integrating the field parallel to the loop over the loop circumference. The $\phi-$directed current on the loop antenna is assumed to take the form

$$I_A = Ae^{-j4\phi}, \tag{4.4}$$

where A is an arbitrary constant. The voltage difference across the loop terminal is thus computed as

$$V_{\text{loop}} = \int_{-\pi}^{\pi} E_\phi(\rho_A, \phi, z) e^{-j4\phi} \rho_A d\phi, \tag{4.5}$$

where

$$E_\phi(\rho_A, \phi, z) = \sum_m a_{4m}^{\text{TM}} E_{\phi,4m}^{\text{TE}+}(\rho_A, \phi, z) + a_{4m}^{\text{TM}} E_{\phi,4m}^{\text{TM}+}(\rho_A, \phi, z), \qquad z = z_A^+. \tag{4.6}$$

The input impedance of the loop antenna is then found as

$$Z_{in,\text{loop}} = \frac{V_{\text{loop}}}{A}. \tag{4.7}$$

4.1.2 Transmission Line Input Impedance Model

Determining the field-based input impedance following the procedure in Section 4.1.1 is doable, yet very involved. But, more importantly, it does not give a good insight on how to design the launcher. Hence, instead of using the field-based method, a phenomenological approach based on transmission line theory that takes into account the correct field behavior is employed. Such an approach yields simpler expressions to evaluate and lucid physical insight without sacrificing accuracy.

In this proposed input impedance model, the effect of the launcher structure is divided into distinct physical contributions and each one is modeled as a terminated TL section. This approach is suitable for the proposed design because the TE_{q1} mode is the only propagating mode inside the waveguide section. Accordingly, the propagation constant of the TL is thus

$$\beta_g = \beta_{q1}^{\mathrm{TE}} = \sqrt{k^2 - (k_{c,q1}^{\mathrm{TE}})^2}, \tag{4.8}$$

and its characteristic impedance is $Z_g = (k/\beta_g)Z_0$, where $Z_0 = 377\,\Omega$ is the free-space impedance.

The input impedance of the loop antenna inside the launcher may be, to a first-order approximation, modeled as a parallel combination of:

1. the free space loop impedance Z_A, which is to be measured through full-wave simulation,
2. a short-circuited TL of length z_A, which models the effect of the closed-end of the waveguide section,

$$Z_{CE} = jZ_g \tan\left(\beta_g z_A\right), \tag{4.9}$$

3. a Z_0 terminated TL of length $z_o = z_G - z_A$, which models the effect of reflection from the open-end,

$$Z_{OE} = \frac{Z_g\left[Z_0 + jZ_g \tan\left(\beta_g z_o\right)\right]}{\left[Z_g + jZ_0 \tan\left(\beta_g z_o\right)\right]}, \tag{4.10}$$

4. a TL terminated by Z_0 in series with $Z_{sc} = jZ_g \tan(\beta_g z_G)$, of length z_o, which models the effect of the reflection from the open-end of the field reflected from the closed-end,

$$Z_R = \frac{Z_g\left[Z_0 + Z_{sc} + jZ_g \tan\left(\beta_g z_o\right)\right]}{\left[Z_g + j[Z_o + Z_{sc}]\tan\left(\beta_g z_o\right)\right]}. \tag{4.11}$$

In addition to the previous contributions, the coupling between the loop antenna and the waveguide may be modeled by a series impedance $Z_{CC} = -2jX_A \sin(\beta_g z_o)$, where X_A is the reactance of the loop antenna in free-space. The input impedance is thus given by

$$Z_{in} = Z_{CC} + \left(\frac{1}{Z_A} + \frac{1}{Z_{CE}} + \frac{1}{Z_{OE}} + \frac{1}{Z_R}\right)^{-1} \tag{4.12}$$

4.1.3 Results

This model uses the following parameter values for calculations: $\lambda = 33.3$ mm, $\lambda_{g,41} = 97.9$ mm, $\beta_g = 64.2$ rad/m, $z_G = 63.7$ mm, $\rho_A = 21.2$ mm, $Z_A = 174 - j58\ \Omega$, $Z_0 = 377\ \Omega$, $Z_g = 1107.2\ \Omega$, and $Z_{sc} = j1529.6\ \Omega$. It is shown that at $z_A = \lambda_{g,q1}/2$ the input resistance drops to zero. This suggests that the optimal choice of z_A is in the vicinity of $\lambda_{g,q1}/2$ such that the resistive part of the input

impedance is $50\,\Omega$. From the expression of Z_{CE}, it is deduced that there are two possible z_A choices resulting in $\mathrm{Re}\{Z_{in}\} = 50\,\Omega$ around $z_A = \lambda_{g,q1}/2$. However, preference is given to the location with inductive reactance, because it is more practical to match using a capacitive load. Optimal Z_{in} value through TL model is found to be $50.1 + j72.6\,\Omega$ for $z_A = 50.5\text{ mm}$. Matching is accomplished by adding a series load reactance that is complex conjugate of the reactive part of the antenna input impedance, which corresponds to a series capacitance of $0.21\,\text{pF}$. Further impact of coarse and fine variations of z_A is demonstrated in this section and Section 4.3.2, respectively.

The simulation is carried out using the default settings of Altair FEKO simulation software. The antenna is constructed as a strip loop using perfect electric conductor (PEC) material with strip width of 0.5 mm. An edge port is used on the antenna feed line with a voltage source of 1 V and $(50 - j80)\,\Omega$ impedance. The waveguide section is constructed using PEC material.

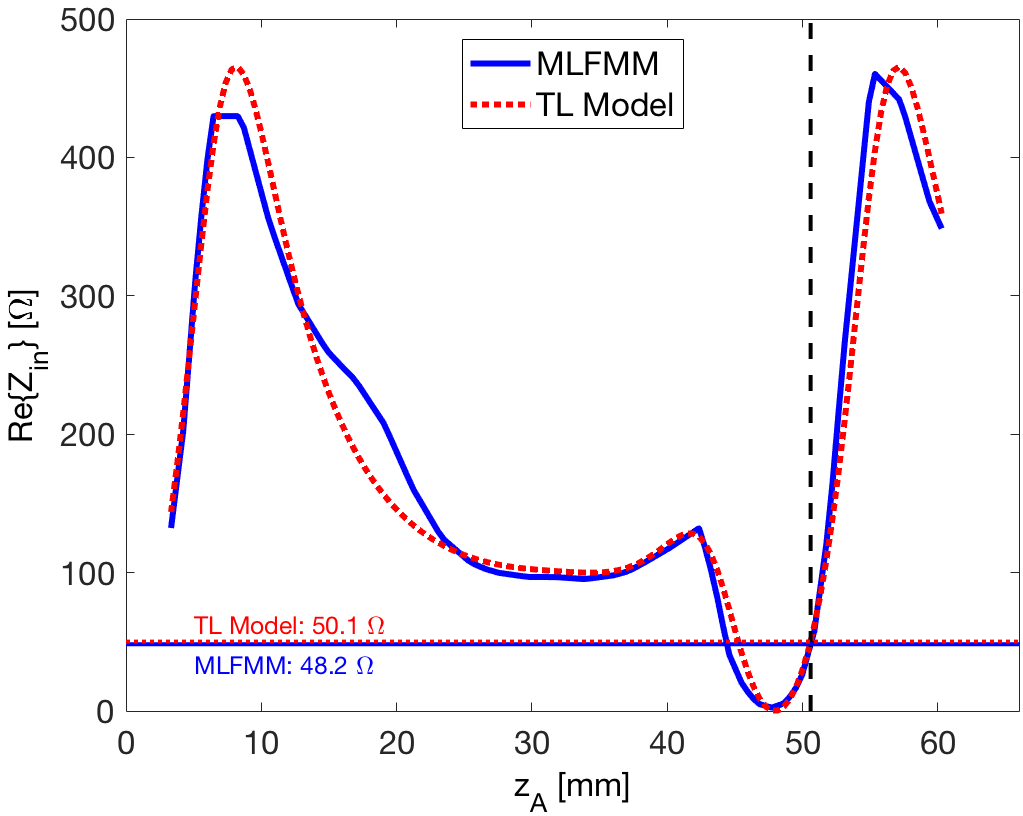

(a)

Figure 4.2 Comparison between full-wave simulation and TL modeling of **(a)** the real part, and **(b)** the imaginary part of the loop antenna input impedance versus its position inside the launcher. The length of the launcher structure is $z_G = 63.7\,\text{mm}$. The radius of the antenna is $\rho_A = 21.2\,\text{mm}$ and the antenna excites the TE_{41} mode at the operation frequency of 9 GHz. (Continued)

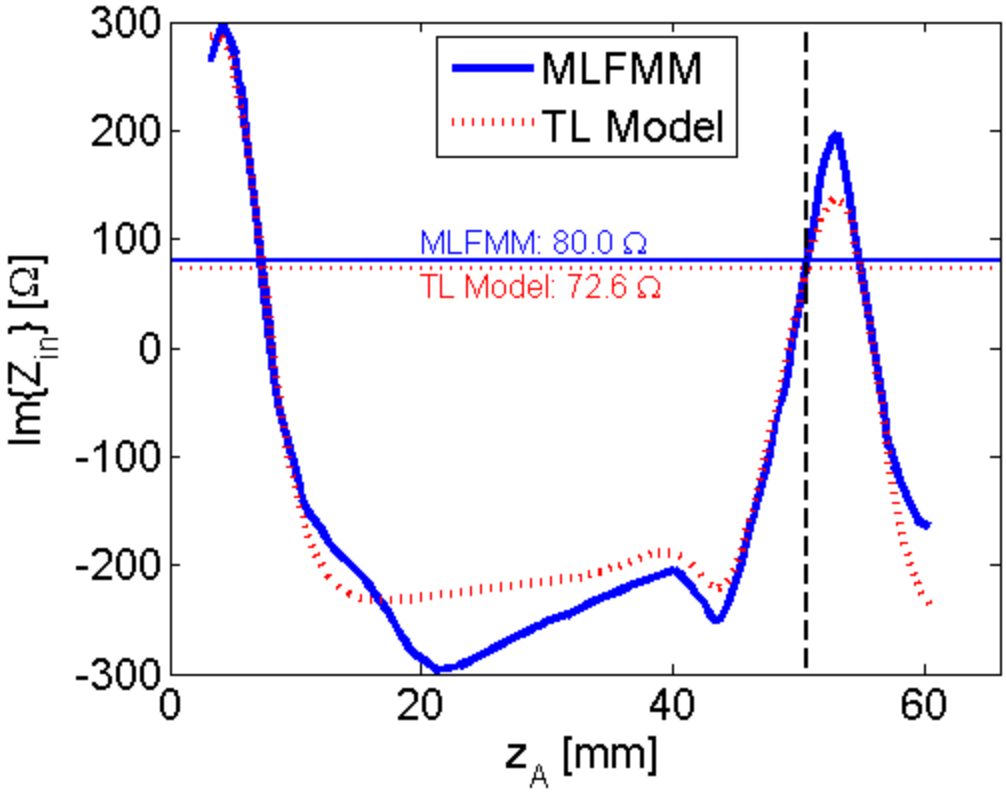

(b)

Figure 4.2 (Continued) Comparison between full-wave simulation and TL modeling of **(a)** the real part, and **(b)** the imaginary part of the loop antenna input impedance versus its position inside the launcher. The length of the launcher structure is $z_G = 63.7\,\text{mm}$. The radius of the antenna is $\rho_A = 21.2\,\text{mm}$ and the antenna excites the TE_{41} mode at the operation frequency of 9 GHz.

Nevertheless, it should be noted that Equation (4.12) is not accurate in estimating the input impedance, specifically its reactance, for locations about $z_A \approx \lambda_g / 4$, which suggests that additional effects should be taken into consideration. This shortcoming, however, does not affect the validity in estimating Z_A near the optimal matching position. Overall, the model provides sound guidelines

to find the optimal antenna location for the best matching performance (hence the best radiation efficiency), as it is shown in Figure 4.2.

In order to establish a relationship between optimal antenna location for ideal impedance matching and waveguide length, z_G is varied within the interval $[55.76\text{ mm}, 90.76\text{ mm}]$ in 2 mm steps and z_A for optimal matching is found after full-wave simulation.

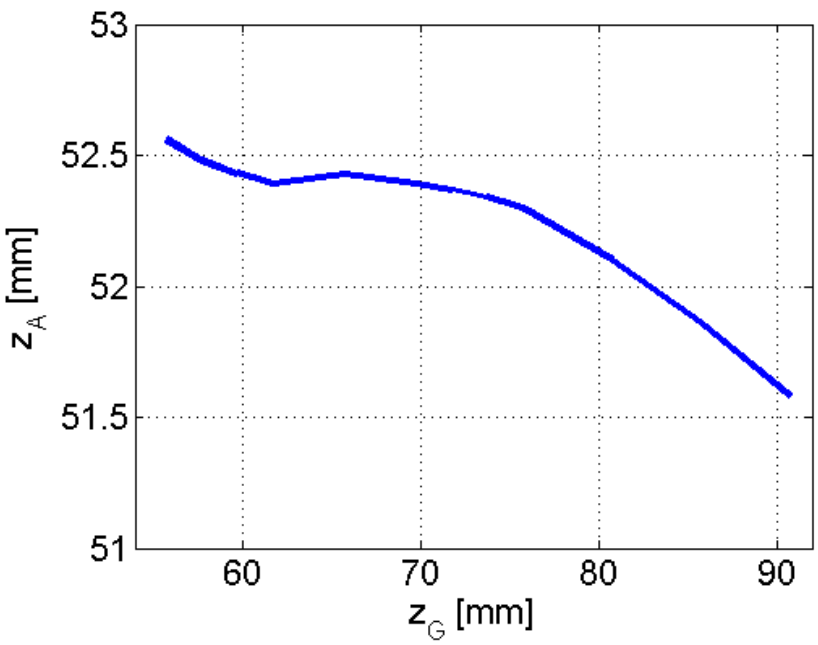

Figure 4.3 Optimal antenna location z_A for different waveguide length z_G. The radius of the waveguide is $a = 30\text{ mm}$, the radius of the antenna is $\rho_A = 21.2\text{ mm}$ and the antenna excites the TE_{41} mode at the operation frequency of 9 GHz.

As illustrated in Figure 4.3, the optimal z_A is almost independent of z_G. This confirms the assertion that z_A almost won't be affected as long as $z_G \geq 0.75\lambda_g$.

4.2 Effect of Flange Angle

It is demonstrated in [54] that introducing a metallic flange at the open end of the waveguide forces the electric field to be zero in the radial direction at $z = 0^+$ and prevents back scattering from the edge. Based on this assumption, a conical metallic flange is added to the launcher design, and its cone angle is varied to observe the effect of the flange angle on the beam directivity.

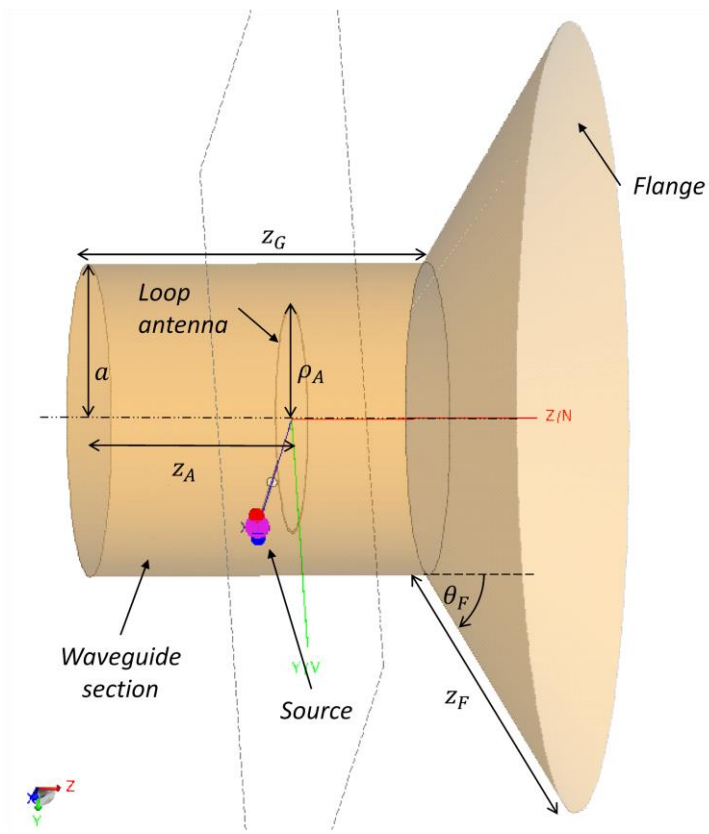

Figure 4.4 Schematic of the vortex beam launcher with a conical flange. The launcher consists of a flanged circular waveguide section with a coaxially-aligned loop antenna.

The flanged launcher design is illustrated in Figure 4.4. The design may bear resemblance to conical horn antennas, which have been extensively studied in the literature [55]. However, studies of radiation performance of conical horn antennas

have exclusively focused on beams not carrying OAM. This may be due to the characteristic on-axis amplitude null of OAM-carrying beams, which translates to conical radiation patterns in the far-field, as illustrated in Figure 3.5. Such conical radiation patterns were traditionally unfavorable for communication applications and thus were not given attention in previous studies.

Nevertheless, with the ongoing interest in radio OAM multiplexing schemes [56], a quantitative understanding of the relationship between the design of vortex beam transceivers and the radiation pattern is essential. Specifically, since boresight communication is, by definition, not viable in OAM multiplexing systems, quantifying the angle of maximum radiation of the transmitter is necessary to optimally place the receiver.

4.2.1 Methodology

In the flanged design, the angle of maximum radiation θ_R depends on the geometry of the launcher, and particularly on the flange angle θ_F. To quantify the effect of θ_F in conjunction with q on θ_R, four test setups are created corresponding to launchers of beams with topological charges $q =$ 3, 4, 5, and 6. Table 4.1 summarizes the launcher design parameters for the test setups. The waveguide radius is fixed at $a = 30$ mm for all test setups.

Table 4.1 Summary of the Launcher Design Parameters

q	λ	ρ_A	z_A	z_G	z_F
3	42.83	20.45	39.67	61.35	40.90
4	33.31	21.22	50.93	63.66	42.44
5	27.25	21.68	32.43	65.04	43.36
6	24.98	23.85	35.30	71.55	47.70

Note: All units are in mm.

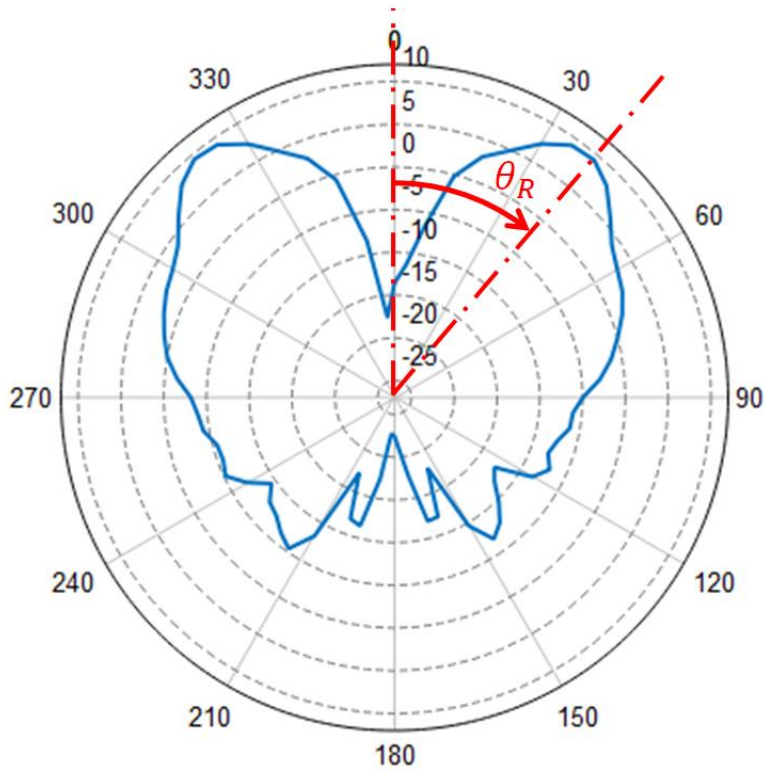

Figure 4.5 Typical gain radiation pattern of a vortex beam with indication of the angle of maximum gain in the main lobe θ_R. The depicted pattern is for a beam with $q = 4$ radiated by a launcher with $\theta_F = 40^\circ$ resulting in $\theta_R = 40^\circ$ in the $\phi = 160^\circ$ plane.

For each one of the launcher setups, full-wave simulation is carried out for $\theta_F = (10p)^\circ$, with $p = 1, 2, \ldots, 9$, and θ_R is measured as the angle of maximum gain in the radiation of the main lobe, as illustrated in Figure 4.5. While the radiation pattern should be symmetric in ϕ, in the simulation results it is not perfectly symmetric due to the geometric asymmetry as seen in Figure 3.5. The simulation used is the multilevel fast multipole method (MLFMM) on the default settings of Altair FEKO simulation software [51].

4.2.2 Results

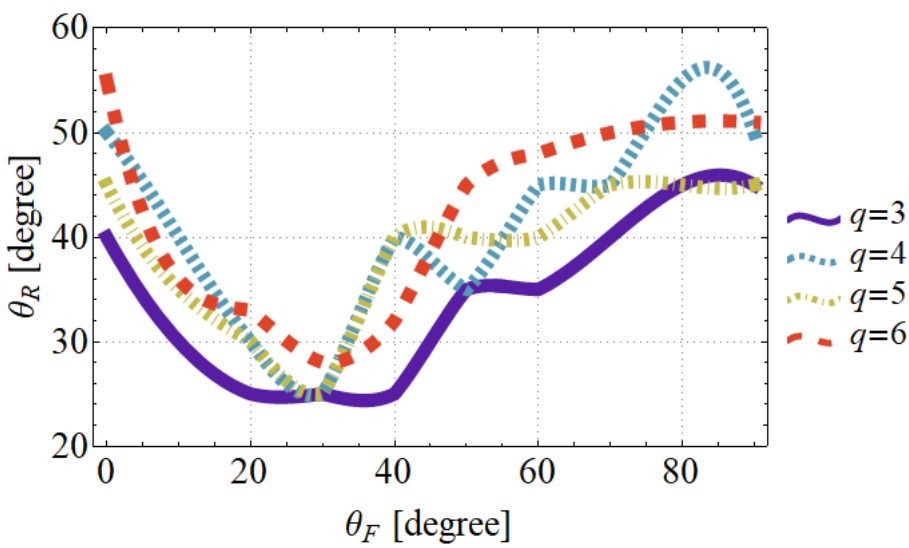

Figure 4.6 Angle of maximum radiation θ_R versus flange angle θ_F, for beams with topological charges $q = 3$, 4, 5, and 6.

Figure 4.6 plots θ_R versus θ_F for the different values of q. The plot shows that θ_R depends on both θ_F and q, where θ_R initially decreases with increasing θ_F until it reaches a certain minimum value, then increases. The pattern of how θ_R changes with θ_F is rather peculiar, since it cannot be readily explained in terms of

the linear momentum of the launched beams. The fact that the effect of θ_F on θ_R depends on q may be an important observation, especially for designing OAM multiplexing communication systems. This result suggests the possibility of designing a launcher for multiple OAM states having the same θ_R, thus allowing for simplified receiver design.

4.3 Sensitivity Analysis

In order to further investigate the launcher performance under small deviations from the optimal design, its sensitivity to three parameters is analyzed. The first parameter is the variation in the location of the antenna within waveguide, the second parameter is the variation in the waveguide length, and the third parameter is the tilt angle of the antenna.

4.3.1 Sensitivity to Variation in Antenna Location

Optimal antenna location within the waveguide is previously found through TL model and MLFMM simulation. In this section, the issue of antenna input impedance sensitivity to small variations around the optimal antenna location is studied. These variations may occur due to placement tolerance and may degrade the performance of the launcher. To this end, the effect of these variations along the $z-$axis on the antenna input impedance as a function of the deviation from the optimal antenna location is analyzed. For practical considerations, it is essential to understand the effect of placement tolerances on the performance of the launcher as they may easily occur while assembling the launcher.

4.3.1.1 Methodology. For optimal matching condition, the antenna is placed at $z_A = 52.4\ \text{mm}$, where its input impedance is estimated as $Z_{in} = 50 + j80\,\Omega$ and can be matched using a 210 fF capacitor. Small deviations about this optimal location are introduced and their corresponding effect on the input impedance is evaluated.

In the performed tests, z_A spans the interval $[45.4\ \text{mm}, 59.4\ \text{mm}]$ and varied in $1\ \text{mm}$ increments, while Z_{in} is measured after full-wave simulation of the launcher. The simulation is carried out using the default settings of Altair FEKO simulation software.

4.3.1.2 Results.

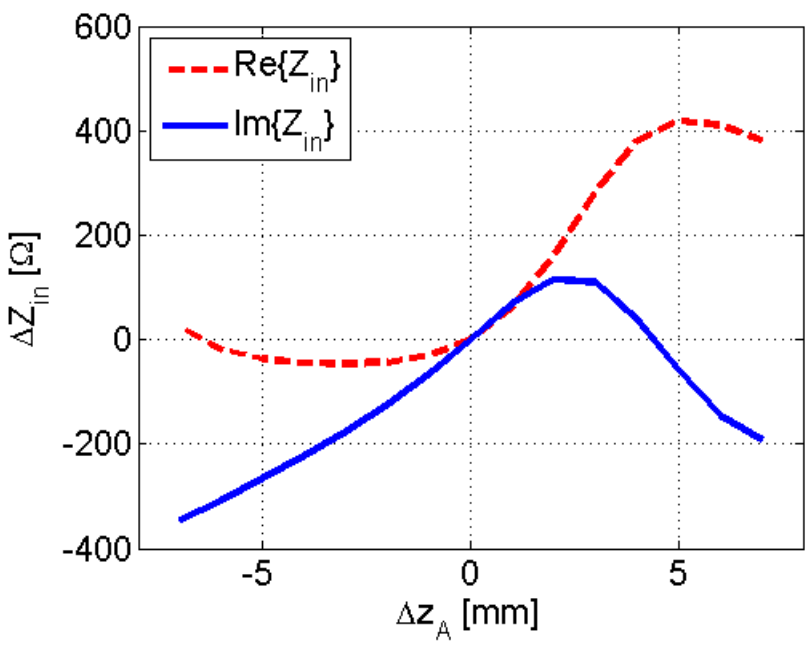

Figure 4.7 Sensitivity of the input impedance Z_{in} to small variations of antenna location around the optimal value $z_A = 52.4\ \text{mm}$.

Figure 4.7 shows that Z_{in} is highly sensitive to variations in z_A. This suggests that in order to achieve the intended performance of the launcher, great care must be given to maintain the design value of z_A. Small shifts from optimal z_A within the range of $\pm 1\,\text{mm}$ about the $z-$axis result in as high as $70\,\Omega$ change in both ΔR_{in} and ΔX_{in}. To be specific, $-1\,\text{mm}$ change results in $\Delta R_{in} = -30\,\Omega$ and $\Delta X_{in} = -70\,\Omega$, which yields a degradation in the radiated power as high as 60%. On the other hand, $+1\,\text{mm}$ change results in $\Delta R_{in} = 70\,\Omega$ and $\Delta X_{in} = 70\,\Omega$, which yields a degradation in the radiated power as high as 30%.

4.3.2 Sensitivity to Variation in Waveguide Length

In this section, the issue of antenna input impedance sensitivity to small variations around the design value of the waveguide length is analyzed. These variations may occur due to fabrication tolerance and may degrade the performance of the launcher. Specifically, the change in input impedance as a function of the deviation in the waveguide length z_G from its design value is studied.

4.3.2.1 Methodology. The next parameter to consider is the effect of the deviation of z_G from its design value on the input impedance of the launcher, since such small deviations in waveguide length may easily occur during the fabrication process. It is thus relevant to quantify the sensitivity of the antenna input impedance to variations in waveguide length around the reference value.

For optimal matching condition determinations, waveguide length reference value is fixed at $z_G = 65.8\,\text{mm}$ and is varied with the interval $[60.8\,\text{mm}, 74.0\,\text{mm}]$ in

$1\,\text{mm}$ steps, while Z_{in} is measured after full-wave simulation of the launcher. The simulation is carried out using the default settings of Altair FEKO simulation software.

4.3.2.2 Results.

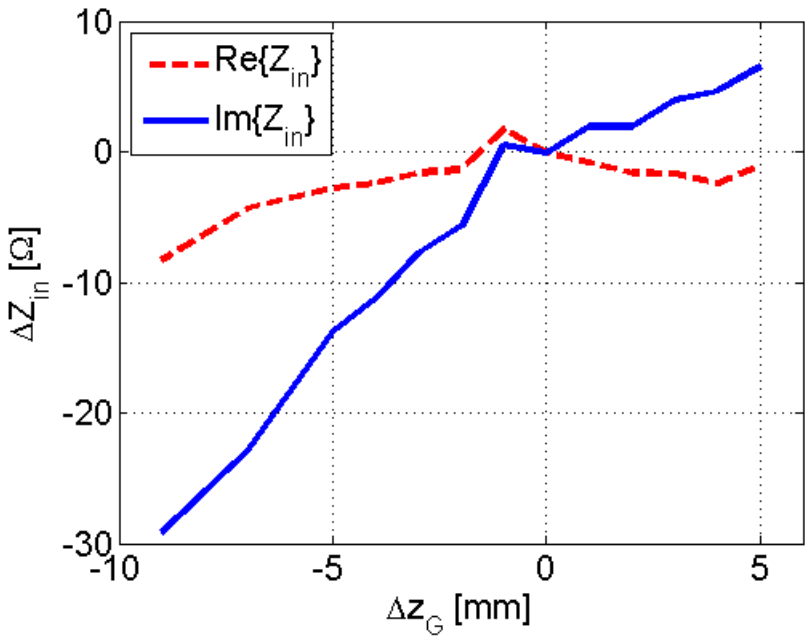

Figure 4.8 Sensitivity of the input impedance Z_{in} to small variations in waveguide length about the reference value $z_G = 65.8\,\text{mm}$.

Figure 4.8 shows that small variations in z_G do not have a big impact on Z_{in}. These results may be understood using the TL model, where z_G plays a secondary role compared to z_A in determining Z_{in}. Shifts from optimal z_G within the range of $\pm 5\,\text{mm}$ about the $z-$axis result in less than $5\,\Omega$ change in ΔR_{in}, however the change in ΔX_{in} is as high as $15\,\Omega$, which yield a degradation in the radiated power less than 3%.

4.3.3 Sensitivity to Antenna Tilt

In this section, the sensitivity of Z_{in} to antenna tilting is established. Antenna tilt may occur due to fabrication tolerance and may degrade the performance of the launcher. To this end, the effect of tilting the antenna along two perpendicular axes is studied, specifically, how the input impedance deviates from its matched value as a function of the tilt angles.

4.3.3.1 Methodology. The antenna tilt is modeled by a Cartesian rotation of the form

$$\begin{bmatrix} x'_a \\ y'_a \\ z'_a \end{bmatrix} = \mathbf{R}\left(\theta_x, \theta_y\right) \begin{bmatrix} x_a \\ y_a \\ z_a \end{bmatrix}, \tag{4.13}$$

where (x_a, y_a, z_a) and (x'_a, y'_a, z'_a) are a point in the plane of the antenna before and after the tilt, respectively, and the rotation matrix is given by

$$\mathbf{R}\left(\theta_x, \theta_y\right) = \begin{bmatrix} \cos(\theta_y) & 0 & \sin(\theta_y) \\ \sin(\theta_x)\sin(\theta_y) & \cos(\theta_x) & -\sin(\theta_x)\cos(\theta_y) \\ -\cos(\theta_x)\sin(\theta_y) & \sin(\theta_x) & \cos(\theta_x)\cos(\theta_y) \end{bmatrix}, \tag{4.14}$$

with θ_x the tilt angle about the $x-$axis, and θ_y the tilt angle about the antenna local $y-$axis. The values of θ_x and θ_y span the interval $\left[-10^\circ, 10^\circ\right]$ in $1°$ steps and Z_{in} is measured after full-wave simulation of the launcher. The simulation is carried out using the default settings of Altair FEKO simulation software.

4.3.3.2 Results.

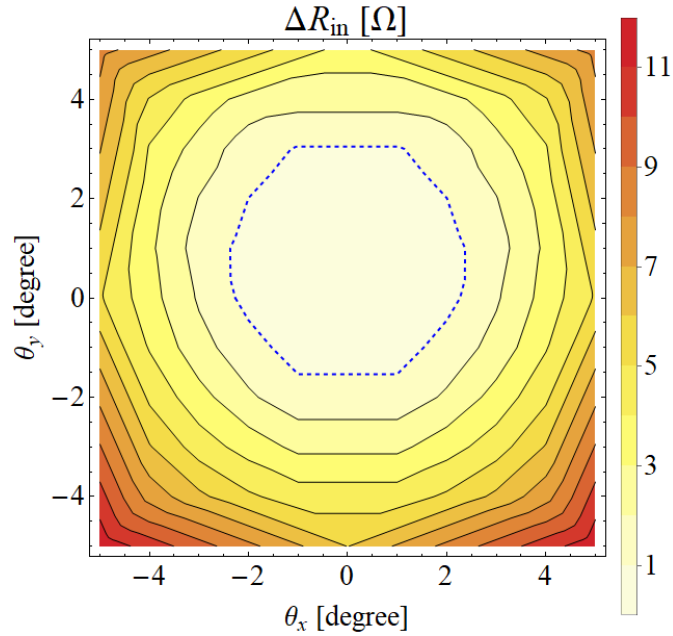

(a)

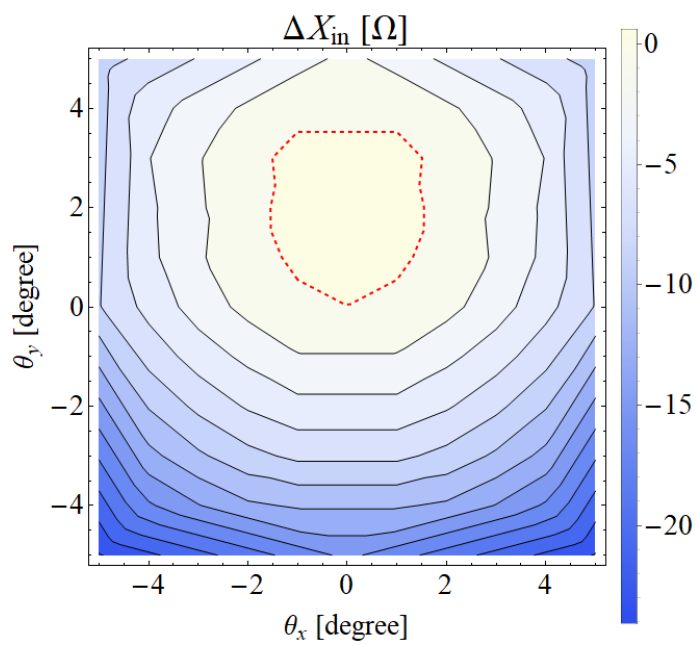

(b)

Figure 4.9 Change in input **(a)** resistance and **(b)** reactance of the antenna with tilt angles θ_x and θ_y. The dashed contours enclose the regions where the change is less than 1Ω.

Figure 4.9 plots the change in Z_{in} as a function in θ_x and θ_y. The dashed contour in Figure 4.9(a) encloses the region where $\Delta R_{in} \leq 1\Omega$, whereas the dashed contour in Figure 4.9(b) encloses the region where $\Delta X_{in} \leq 1\Omega$. It is worthwhile noting that both ΔR_{in} and ΔX_{in} are asymmetric with respect to θ_y. Moreover, ΔX_{in} is more sensitive to tilting and exhibits stronger asymmetry compared to ΔR_{in}. The asymmetry in the behavior is due to the feed line that extends along the antenna local $x-$axis. This particular setup creates an asymmetry about the antenna $y-$axis. The stronger sensitivity of ΔX_{in} is due to the additional coupling between the tilted feed line and the waveguide wall. It is also worthwhile noting that $\Delta R_{in} > 0$, while $\Delta X_{in} < 0$ for all angles. The increase in R_{in} may be understood in terms of the decreased current flow through the antenna, whereas the decrease in ΔX_{in} may be understood in terms of the increased capacitive coupling between the feed line and the waveguide wall.

The plots in Figure 4.9 suggest that the proposed launcher design is robust to small tilts in its antenna. Tilts within the range of $\pm 2^\circ$ about the $x-$axis with a tilt of up to $+3^\circ$ about the antenna local $y-$axis result in ΔR_{in} and ΔX_{in} less than 1Ω, which yield a degradation in the radiated power less than 0.1%. For a radiation power degradation of 10%, the launcher may tolerate a tilt up to $\pm 4^\circ$ about the x-axis with a tilt between -5° and $+10^\circ$ about the local $y-$axis.

CHAPTER 5

CONCLUSIONS AND FUTURE WORK

5.1 Conclusions

This study proposed a new system for launching electromagnetic vortex beams and provided a comprehensive perspective into the practical aspects associated with the proposed launching system. Performance of the proposed launcher is verified through modal analysis and full-wave simulation.

The design objective is to launch a single-mode vortex beam. Performed modal analysis confirms this objective. Hence, the topological charge and the truncated Bessel profile of the excited mode are carried by the launched vortex beam. While a single antenna design results in single mode excitation in the proposed design, generalization to multiple antennas and multimode operation is straightforward.

Two different input impedance models are presented in Chapter 4: (i) field-based model and (ii) the approximate model. The approximate model, which is based on transmission line theory, gives good insight into the impedance behavior of the launcher. The aforementioned transmission line model provides a simplified and computationally efficient approach to find the optimal antenna location for impedance matching within the waveguide, as compared to the field-based analytical model or full-wave simulations. However, this simplified model seems to miss a certain contribution that affects its accuracy of predicting the input impedance when located between the waveguide closed-end and a distance equal to one quarter of the

propagating mode guided wavelength. This inaccuracy, however, does not reduce the usefulness of the model, since the optimal antenna location is, generally speaking, around one half of the propagating mode guided wavelength away from the waveguide closed-end.

For the rest of Chapter 4, the following sensitivity analyses were performed: sensitivity to variation in antenna location, sensitivity to variation in waveguide length, and sensitivity to antenna tilt. These analyses provide an understanding of the expected performance degradation introduced by machinery and human error during the manufacturing and assembly of the launcher structure. This launcher design is particularly sensitive to small variations in antenna location and waveguide length. Small variations in either may greatly change the input impedance accordingly the overall radiation performance. The launcher is found to be robust to small tilts in its antenna.

Overall, the proposed system is shown to be suitable to generate vector vortex beams in the microwave regime. Mode powers calculated through modal analysis confirm the generation of a single mode, which is the intended mode. Compact structure of the launcher and high purity of the launched vortex beam are the advantages of this system. As a common limitation of all OAM-based communication systems, the proposed system cannot be used for boresight communication. This is due to the characteristic magnitude null at the center of OAM beams. The proposed system may be used as a part of a multiplexing scheme in a wireless communication network in order to increase channel capacity. Since the proposed system requires the loop to be placed at a specific spot within the waveguide for optimal performance and

the waveguide length also affects the matching performance, any deviation from the optimal values due to production and assembly errors will reduce the performance.

5.2 Future Work

An important aspect of the launcher design is the generation of a vortex beam with a specific directivity profile. A specific directivity profile can be launched by exciting multiple modes using multiple antennas placed in the launcher structure. In the case of multiple-mode excitation, a similar modal analysis method to the one employed in this study can be applied to a vortex beam which is a superposition of multiple modes. Investigation of the effects of multiple mode excitation on the practical aspects is of importance, as it will give insights on the practical realization of the launching system.

The practical realization of a vortex beam launcher based on the proposed method may require additional investigations into different practical aspects that are not directly related to the electromagnetic performance of the launcher. Such aspects may include the non-linearity effects of the power source, thermal deformations due to operation at high power levels, and mechanical stresses in the launcher structure along with the human and machinery error introduced by the launcher production/assembly process.

As an important part of the practical aspects, the demonstrated input impedance models can be generalized to accommodate different configurations of the launching structure, including multiple antennas.

It is also worthwhile to study the effects of filling the waveguide with dielectric material on the system performance. Specifically, the use of metamaterials to enhance the performance of the launcher or reduce its size may be of interest.

REFERENCES

1. J. H. Poynting, "*The wave motion of a revolving shaft, and a suggestion as to the angular momentum in a beam of circularly polarised light,*" Proc. R. Soc. Lond., A Contain. Pap. Math. Phys. Character **82(557)**, pp. 560–567 (1909).

2. C. G. Darwin, "*Notes on the theory of radiation,*" Proc. R. Soc. Lond., A Contain. Pap. Math. Phys. Character **136(829)**, pp. 36–52 (1932).

3. L. Allen, M. W. Beijersbergen, R. J. C. Spreeuw, and J. P. Woerdman, "*Orbital angular momentum of light and the transformation of Laguerre-Gaussian laser modes,*" Phys. Rev. A **45(11)**, pp. 8185–8189 (1992).

4. P. Coullet, G. Gil, and F. Rocca, "*Optical vortices,*" Opt. Commun. **73(5)**, pp. 403–408 (1989).

5. M. W. Beijersbergen, L. Allen, H. E. L. O. van der Veen, and J. P. Woerdman, "*Astigmatic laser mode converters and transfer of orbital angular momentum,*" Opt. Commun. **96(1-3)**, pp. 123–132 (1993).

6. M. W. Beijersbergen, R. P. C. Coerwinkel, M. Kristensen, and J. P. Woerdman, "*Helical-wavefront laser beamsproduced with a spiral phaseplate,*" Opt. Commun. **112(5-6)**, pp. 321–327 (1994).

7. V. Y. Bazhenov, M. V. Vasnetsov, and M. S. Soskin, "*Laser-beams with screw dislocations in their wave-fronts,*" JETP Lett. **52**, pp. 429–431 (1990).

8. N. Radwell, R. D. Hawley, J. B. Götte, and S. Franke-Arnold, "*Achromatic vector vortex beams from a glass cone,*" Nat. Commun. **7**, 10564 (2016).

9. A. Jesacher, A. Schwaighofer, S. Fürhapter, C. Maurer, S. Bernet, and M. Ritsch-Marte,"*Wavefront correction of spatial light modulators using an optical vortex image,*" Opt. Express **15(9)**, pp. 5801–5808 (2007).

10. M. Mirhosseini, O. S. Magaña-Loaiza, C. Chen, B. Rodenburg, M. Malik, and R. W. Boyd, "*Rapid generation of light beams carrying orbital angular momentum,*" Opt. Express **21(25)**, pp. 30196–30203 (2013).

11. X. Cai, J. Wang, M. J. Strain, B. Johnson-Morris, J. Zhu, M. Sorel, J. L. O'Brien, M. G. Thompson, and S. Yu, "*Integrated compact optical vortex beam emitters,*" Science **338(6105)**, pp. 363–366 (2012).

12. H. He, M. E. J. Friese, N. R. Heckenberg, and H. Rubinsztein-Dunlop, "*Direct observation of transfer of angular momentum to absorptive particles from a laser beam with a phase singularity,*" Phys. Rev. Lett. **75(5)**, pp. 826–829 (1995).

13. J. E. Curtis, B. A. Koss, and D. G. Grier, "*Dynamic holographic optical tweezers,*" Opt. Commun. **207(1-6)**, pp. 169–175 (2002).

14. M. Padgett and R. Bowman, "*Tweezers with a twist,*" Nat. Photonics **5(6)**, pp. 343–348 (2011).

15. S. Ngcobo, I. Litvin, L. Burger, and A. Forbes, "*A digital laser for on-demand laser modes,*" Nat. Commun. **4**, p. 2289 (2013).

16. K. O'Holleran, M. J. Padgett, and M. R. Dennis, "*Topology of optical vortex lines formed by the interference of three, four, and five plane waves,*" Opt. Express **14(7)**, pp. 3039–3044 (2006).

17. M. Uchida and A. Tonomura, "*Generation of electron beams carrying orbital angular momentum,*" Nature **464(7289)**, pp. 737–739 (2010).

18. J. Verbeeck, H. Tian, and P. Schattschneider, "*Production and application of electron vortex beams,*" Nature **467(7313)**, pp. 301–304 (2010).

19. B. J. McMorran, A. Agrawal, I. M. Anderson, A. A. Herzing, H. J. Lezec, J. J. McClelland, and J. Unguris, "*Electron vortex beams with high quanta of orbital angular momentum,*" Science **331(6014)**, pp. 192–195 (2011).

20. B. A. Garetz, "*Angular Doppler effect,*" J. Opt. Soc. Am. **71(5)**, pp. 609–611 (1981).

21. A. Mair, A. Vaziri, G. Weihs, and A. Zeilinger, "*Entanglement of the orbital angular momentum states of photons,*" Nature **412(6844)**, pp. 313–316 (2001).

22. A. Vaziri, G. Weihs, and A. Zeilinger, "*Superposition for the orbital angular momentum for applications in quantum experiments,"* J. Optics B **4**, pp. 547-551 (2002).

23. G. A. Swartzlander, Jr., E. L. Ford, R. S. Abdul-Malik, L. M. Close, M. A. Peters, D. M. Palacios, and D. W. Wilson, "*Astronomical demonstration of an optical vortex coronagraph,*" Opt. Express **16(14)**, pp. 10200–10207 (2008).

24. S. Fürhapter, A. Jesacher, S. Bernet, and M. Ritsch-Marte, "*Spiral interferometry,*" Opt. Lett. **30(15)**, pp. 1953–1955 (2005).

25. S. R. P. Pavani and R. Piestun, "*Three dimensional tracking of fluorescent microparticles using a photon-limited double-helix response system,*" Opt. Express **16(26)**, pp. 22048–22057 (2008).

26. A. Jesacher, M. Ritsch-Marte, and R. Piestun, "*Three-dimensional information from two-dimensional scans: a scanning microscope with post acquisition refocusing capability,*" Optica **2(3)**, pp. 210–214 (2015).

27. F. Tamburini, E. Mari, A. Sponselli, B. Thidé, A. Bianchini, and F. Romanato, "*Encoding many channels on the same frequency through radio vorticity: first experimental test,*" New J. Phys. **14(3)**, p. 033001 (2012).

28. M. Tamagnone, C. Craeye, and J. Perruisseau-Carrier, "*Comment on 'Encoding many channels on the same frequency through radio vorticity: first experimental test,*" New J. Phys. **14(11)**, p. 118001 (2012).

29. F. Tamburini, E. Mari, A. Sponselli, B. Thidé, A. Bianchini, and F. Romanato, "*Reply to Comment on 'Encoding many channels on the same frequency through radio vorticity: first experimental test,*" New J. Phys. **14(11)**, p. 118002 (2012).

30. Y. Yan, G. Xie, M. P. J. Lavery, H. Huang, N. Ahmed, C. Bao, Y. Ren, Y. Cao, L. Li, Z. Zhao, A. F. Molisch, M. Tur, M. J. Padgett, and A. E. Willner, "*High-capacity millimetre-wave communications with orbital angular momentum multiplexing,*" Nat. Commun. **5**, p. 4876 (2014).

31. X. Hui, S. Zheng, Y. Chen, Y. Hu, X. Jin, H. Chi, and X. Zhang, "*Multiplexed millimeter wave communication with dual orbital angular momentum (OAM) mode antennas,*" Sci. Rep. **5**, p. 10148 (2015).

32. S. Li and J. Wang, "*Performance evaluation of analog signal transmission in an orbital angular momentum multiplexing system,*" Opt. Lett. **40**, pp. 760-764 (2015).

33. L. Zhu, J. Li, G. Zhu, C. Cai, M. Tang, Z. He, S. Yu, C. Du, W. Luo, J. Liu, and J. Du, "*First Demonstration of Orbital Angular Momentum (OAM) Distributed Raman Amplifier over 18-km OAM Fiber with Data-Carrying OAM Multiplexing and Wavelength-Division Multiplexing,*" Opt. Fib. Commun. Conf., **W4C-4** (2018).

34. A. F. Morabito, L. Di Donato and T. Isernia, "*Orbital Angular Momentum Antennas: Understanding Actual Possibilities through the Aperture Antennas Theory,*" IEEE Ant. & Prop. Mag., **60(2)**, pp. 59-67 (2018).

35. M. Veysi, C. Guclu, F. Capolino and Y. Rahmat-Samii, "*Revisiting Orbital Angular Momentum Beams: Fundamentals, Reflectarray Generation, and Novel Antenna Applications,*" IEEE Ant. & Prop. Mag., **60(2)**, pp. 68-81 (2018).

36. M. W. Beijersbergen, R. P. C. Coerwinkel, M. Kristensen, and J. P. Woerdman, "*Helical-wavefront laser beams produced with a spiral phase plate,*" Opt. Commun. **112(5–6)**, p. 321 (1994).

37. V. Yu. Bazhenov, M. V. Vasnetsov, and M. S. Soskin, "*Laser beams with screw dislocations in their wavefronts,*" JETP Lett. **52(8)**, pp. 429–431 (1990).

38. M. Gecevicius, R. Drevinskas, M. Beresna, and P. G. Kazansky, "*Single beam optical vortex tweezers with tunable orbital angular momentum,*" Appl. Phys. Lett. **104(23)**, p. 231110 (2014).

39. C. Deng, W. Chen, Z. Zhang, Y. Li, and Z. Feng, "*Generation of OAM Radio Waves Using Circular Vivaldi Antenna Array,*" Int. J. Ant. Prop. **2013**, p. 847859 (2013).

40. W. J. Byun, K. S. Kim, B. S. Kim, Y. S. Lee, M. S. Song, H. D. Choi, and Y. H. Cho, "*Multiplexed Cassegrain reflector antenna for simultaneous generation of three orbital angular momentum (OAM) modes,*" Sci. Rep. **6**, p. 27339 (2016).

41. N. Kou, S. Yu, and L. Li, "*Generation of high-order Bessel vortex beam carrying orbital angular momentum using multilayer amplitude-phase-modulated surfaces in radiofrequency domain,*" Appl. Phys. Express **10(1)**, p. 016701 (2017).

42. A. M. Yao and M. J. Padgett, "*Orbital angular momentum: origins, behavior and applications*," Adv. Opt. Photon., **3(2)**, pp. 161-204 (2011).

43. J. Durnin, "*Exact solutions for nondiffracting beams, I. the scalar theory*," J. Opt. Soc. Am. A, **4(4)**, pp. 651-654 (1987).

44. M. A. Salem and C. Caloz, "*Localized Waves: Theory, Techniques, and Applications*," in Handbook of Antenna Technologies, Z. Chen, D. Liu, H. Nakano, X. Qing, and T. Zwick (Eds), Springer, pp. 567-618 (2016).

45. G. Goubau and F. Schwering, "*On the guided propagation of electromagnetic wave beams*," IRE Trans. on Ant. & Prop., **9(3)**, pp. 248-256 (1961).

46. L. Allen, M. W. Beijersbergen, R. J. C. Spreeuw, and J. P. Woerdman, "*Orbital angular momentum of light and the transformation of Laguerre-Gaussian laser modes*," Phys. Rev. A, **45**(11), p. 8185 (1992).

47. S. M. Barnett, M. Babiker, and M. J. Padgett, "*Optical orbital angular momentum*," Phil. Trans. Ser. A, Math., Phys., & Eng. Sci., **375(2087)**, p. 20150444 (2017).

48. A. T. O'Neil, I. MacVicar, L. Allen, and M. J. Padgett, "*Intrinsic and Extrinsic Nature of the Orbital Angular Momentum of a Light Beam*," Phys. Rev. Lett. **88**, p. 053601 (2002).

49. R. E. Collin, "*Field theory of guided waves*," IEEE Press 2nd ed., pp. 358-362 (1991).

50. D. M. Pozar, "*Microwave Engineering*," John Wiley & Sons 4th ed., pp. 122-126 (2011).

51. Altair, "*FEKO Overview,*" https://altairhyperworks.com/product/FEKO, accessed 24 July 2018.

52. C. A. Balanis, "*Antenna Theory: Analysis and Design*," John Wiley 4th ed., pp. 256-259 (2016).

53. P. S. Carter, "*Circuit Relations in Radiating Systems and Applications to Antenna Problems,*" Proc. IRE **20(6)**, pp. 1004-1041 (1932).

54. M. A. Salem, A. H. Kamel, and E. Niver, "*Microwave Bessel beams generation using guided modes,*" IEEE Trans. Ant. Prop., **59(6)**, pp. 2241–2247 (2011).

55. A. P. King, "*The radiation characteristics of conical horn antennas,*" Proc. IRE, vol. **38(3)**, pp. 249–251 (1950).

56. D. Lee, H. Sasaki, H. Fukumoto, K. Hiraga, and T. Nakagawa, "*Orbital angular momentum (OAM) multiplexing: An enabler of a new era of wireless communications,*" IEICE Trans. Commun., **E100-B(7)**, pp. 1044–1063 (2017).